Progress in Oceanography 219 (2023) 103169

Contents lists available at ScienceDirect

Progress in Oceanography

journal homepage: www.elsevier.com/locate/pocean

The Pacific water flow branches in the eastern Chukchi Sea

Robert S. Pickart [a,*], Peigen Lin [b,a], Frank Bahr [a], Leah T. McRaven [a], Jie Huang [a], Astrid Pacini [c], Kevin R. Arrigo [d], Carin J. Ashjian [a], Catherine Berchok [e], Mark F. Baumgartner [a], Kyoung-Ho Cho [f], Lee W. Cooper [g], Seth L. Danielson [h], Douglas Dasher [h], Amane Fuiwara [i], Jeanette Gann [r], Jacqueline M. Grebmeier [g], Jianfeng He [j], Toru Hirawake [k], Motoyo Itoh [i], Lauren Juranek [n], Takashi Kikuchi [i], G.W.K. Moore [l], Jeff Napp [e], R. John Nelson [q], Shigeto Nishino [i], Hank Statscewich [h], Phyllis Stabeno [m], Kathleen M. Stafford [o], Hiromichi Ueno [p], Svein Vagle [q], Thomas J. Weingartner [h], Bill Williams [q], Sarah Zimmermann [q]

[a] *Woods Hole Oceanographic Institution, Woods Hole, MA 02543, USA*
[b] *Shanghai Jiao Tong University, School of Oceanography, Shanghai 200030, China*
[c] *University of Washington, Applied Physics Laboratory, Polar Science Center, 1013 NE 40th Street, Seattle, WA 98105-669, USA*
[d] *Stanford University, Department of Earth System Science, 473 Via Ortega, Stanford, CA 94305-2215, USA*
[e] *NOAA Fisheries, Alaska Fisheries Science Center, 76600 Sand Point Way N.E, Seattle, WA 98115, USA*
[f] *Korea Polar Research Institute (KOPRI), 26, Songdomirae-ro, Yeonsu-gu, Incheon 406-840, South Korea*
[g] *Chesapeake Biological Laboratory, University of Maryland Center for Environmental Science, Solomons, MD 20688, USA*
[h] *University of Alaska Fairbanks, School of Fisheries and Ocean Sciences, Seward Marine Center, P.O. Box 757220, Fairbanks, AK 99775, USA*
[i] *Japan Agency for Marine-Earth Science and Technology (JAMSTEC), 2-15 Natsushima-cho, Yokosuka, Kanagawa 237-0061, Japan*
[j] *Polar Research Institute of China, 451 Jinqiao Rd, Shanghai 201209, China*
[k] *National Institute of Polar Research, Japan, 10-3, Midori-cho, Tachikawa-shi, Tokyo 190-8518, Japan*
[l] *Department of Physics, University of Toronto, Toronto, ON M5S 1A7, Canada*
[m] *Pacific Marine Environmental Laboratory, National Oceanic and Atmospheric Administration, Seattle, WA, USA*
[n] *College of Earth, Ocean and Atmospheric Sciences, Oregon State University, Corvallis, OR 97331, USA*
[o] *Marine Mammal Institute, Oregon State University 2030 SE Marine Science Dr, Newport, OR 97365, USA*
[p] *Hokkaido University, 3-1-1 Minato-cho, Hakodate 041-8611, Japan*
[q] *Fisheries and Oceans Canada, Institute of Ocean Sciences, 9860 West Saanich Road, Sidney, BC V8L 4B2, Canada*
[r] *NOAA Fisheries, Alaska Fisheries Science Center, 17109 Point Lena Loop Rd, Juneau, AK 99801, USA*

ARTICLE INFO

Keywords:
Boundary currents
Arctic Ocean
Chukchi Sea circulation
Water masses
Alaskan Coastal Current
Bering Strait
Barrow Canyon

ABSTRACT

The flow of Pacific-origin water across the Chukchi Sea shelf impacts the regional ecosystem in profound ways, yet the two current branches on the eastern shelf that carry the water from Bering Strait to Barrow Canyon – the Alaskan Coastal Current (ACC) and Central Channel (CC) Branch – have not been clearly distinguished or quantified. In this study we use an extensive collection of repeat hydrographic sections occupied at three locations on the Chukchi shelf, together with data from a climatology of shipboard velocity data, to accomplish this. The data were collected predominantly between 2010 and 2020 during the warm months of the year as part of the Distributed Biological Observatory and Arctic Observing Network. The mean sections show that mass is balanced for both currents at the three locations: Bering Strait, Point Hope, and Barrow Canyon. The overall mean ACC transport is 0.34 ± 0.04 Sv, and that of the CC Branch is 0.86 ± 0.11 Sv. The dominant hydrographic variability at Bering Strait is seasonal, but this becomes less evident to the north. At Barrow Canyon, the dominant hydrographic signal is associated with year-to-year variations in sea-ice melt. Farther south there is pronounced mesoscale variability: an empirical orthogonal function analysis at Bering Strait and Point Hope reveals a distinct ACC mode and CC Branch mode in hydrography and baroclinic transport, where the former is wind-driven. Finally, the northward evolution in properties of the two currents is investigated. The poleward increase in salinity of the ACC can be explained by lateral mixing alone, but solar heating together with wind mixing play a large role in the temperature evolution. This same atmospheric forcing also impacts the northward evolution of the CC Branch.

* Corresponding author.
E-mail address: rpickart@whoi.edu (R.S. Pickart).

https://doi.org/10.1016/j.pocean.2023.103169
Received 29 June 2023; Received in revised form 31 October 2023; Accepted 4 November 2023
Available online 10 November 2023
0079-6611/Crown Copyright © 2023 Published by Elsevier Ltd. This is an open access article under the CC BY-NC license (http://creativecommons.org/licenses/by-nc/4.0/).

1. Introduction

Pacific-origin water follows several pathways across the Chukchi shelf from Bering Strait to the deep interior basin, impacting the regional ecosystem in profound ways. In the summer months the warm water contributes to ice melt and provides freshwater that increases the stratification in the upper water column. This in turn helps trap phytoplankton near the surface, resulting in large blooms on the Chukchi shelf (Anderson et al., 2021). The Pacific-origin summer water is also a major contributor to the Beaufort Gyre freshwater reservoir (Proshutinsky et al., 2019). During the cold months of the year, ice formation in the northern Bering and Chukchi Seas results in brine-driven convective overturning and the formation of near-freezing water. When the overturning reaches the bottom, it stirs nutrients from the sediments into the water column (Cooper et al., 1997; Lowry et al., 2018; Pacini et al., 2019). The resulting high-nutrient winter water subsequently fuels early season primary production on the Chukchi shelf (Lowry et al., 2015). The winter water also ventilates the cold halocline in the Canada Basin (Aagaard et al., 1981), which helps prohibit the underlying warm Atlantic water from mixing upwards to the surface, in which case it would cause significant ice melt.

The three main flow branches of Pacific-origin water on the Chukchi shelf are the western pathway that flows through Herald Canyon, the middle pathway that flows through Central Channel, and the eastern pathway adjacent to the Alaskan coast (Fig. 1). The latter is referred to as the Alaskan Coastal Current during the summer months (Paquette and Bourke, 1974; Weingartner et al., 1999) as it advects warm, fresh continental runoff to the north. The division in transport between these three branches, as well as the precise fate of each pathway, remain uncertain. For instance, the portion of the western branch flowing into the East Siberian Sea through Long Strait versus that flowing northward through Herald Canyon has yet to be quantified. Woodgate et al. (2005) estimated 0.1–0.3 Sv for each pathway, but that was based on only a single mooring in Long Strait and at the mouth of Herald Canyon. A synoptic shipboard survey of Herald Canyon revealed that some of the canyon outflow turns eastward on the north side of Herald Shoal, while the remaining part forms the Chukchi Shelfbreak Jet (Fig. 1) (Pickart et al., 2010).

The middle branch, after passing through Central Channel, is thought to split into filaments. Some of the flow turns eastward immediately after exiting the channel, while the remaining portion divides again as it encounters Hanna Shoal (Fig. 1). The general eastward progression of the filamented middle branch is supported by shipboard hydrographic and velocity measurements (Weingartner et al., 2005; Pickart et al., 2016; Pacini et al., 2019; Lin et al., 2019), mooring data (Fang et al., 2020; Tian et al., 2021; Stabeno and McCabe, 2023), and drifter data (Stabeno and McCabe, 2023). However, it remains uncertain if all of the flow in the middle branch ultimately exits the Chukchi shelf through Barrow Canyon. For instance, there is evidence of northward outflow through Hanna Canyon (Spall et al., 2018). The Alaskan Coastal Current is readily identified by its hydrographic properties north of Bering Strait, but the transport of this branch of Pacific-origin water has also not been well quantified observationally. This is partly due to the frequent upwelling-favorable northerly winds in the region which can hinder or reverse the flow (Danielson et al., 2017; Lin et al., 2019) and cause some of the water to spread into the interior Chukchi shelf (e.g., Danielson et al., 2017; Pisareva et al., 2019; Li et al., 2021).

Among the many moorings deployed over the years on the eastern Chukchi shelf, three long-term arrays in particular have enabled estimates of the net poleward transport of Pacific-origin water (see Fig. 1 for the mooring locations). The first is the Bering Strait array which has been deployed in various configurations since 1990 and is now part of

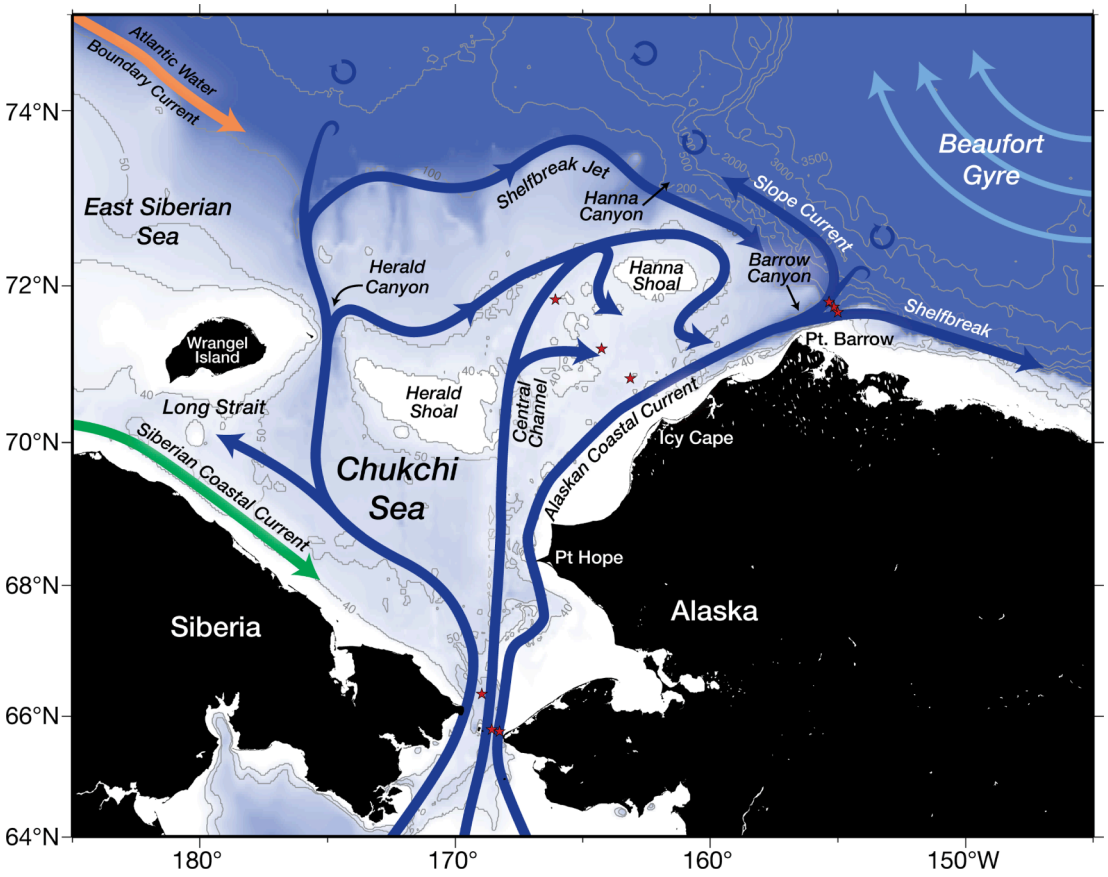

Fig. 1. Schematic circulation of the Chukchi Sea with place names (after Corlett & Pickart, 2017). The red stars denote the mooring locations comprising the three arrays discussed in the Introduction: Bering Strait; Icy Cape; mouth of Barrow Canyon. The bottom topography (in meters) is from ETOPO-2.

the Arctic Observing Network (Woodgate, 2018). The second is the Ecosystems & Fisheries-Oceanography Coordinated Investigations (EcoFOCI) array, deployed in 2010, which consists of three moorings situated seaward of Icy Cape (Stabeno and McCabe, 2023). The third such array is the Japan Agency for Marine-Earth Science and Technology (JAMSTEC) array at the mouth of Barrow Canyon which has been deployed since 2000 (Itoh et al., 2013). Generally speaking, the northward volume transports of Pacific-origin water estimated using these long-term timeseries tell a consistent story.

Over the approximately three decades that the Bering Strait array has been in the water, the annual mean volume transport (across the entire strait) has increased by roughly 25% and is now 1 ± 0.05 Sv (Woodgate, 2018). Seasonally, the largest transport, 1.45 ± 0.14 Sv, occurs in June. Based on the three EcoFOCI moorings deployed offshore of Icy Cape (centered near 71°N), the annual mean northward transport is 0.43 Sv, with a peak monthly mean value of 0.75 Sv in July (Stabeno and McCabe, 2023). The annual mean northward transport at the mouth of Barrow canyon is estimated to be 0.44 Sv (Itoh et al., 2013), which is nearly identical to the value at the Icy Cape line. While the maximum monthly transport at the canyon mouth also occurs in July, its value is estimated to be somewhat larger, 1.06 Sv, than that calculated at the Icy Cape line. Taken together, these long-term timeseries imply that, averaged over the year, roughly 45% of the total Bering Strait inflow progresses northward on the eastern part of the Chukchi shelf (i.e., east of the US/Russian Convention Line) and flows through Barrow Canyon. In the summer months this percentage is higher, although more uncertain (52–73%).

The mooring data, however, are unable to resolve the middle flow branch and the Alaskan Coastal Current (the eastern-most mooring in Bering Strait is situated in the coastal branch so it does provide information about the flow, but does not resolve it). Furthermore, the hydrographic sensors on the moorings are largely confined to the deep part of the water column. Hence, basic questions remain regarding the division of volume transport between these two Pacific-origin flow branches, the evolution of water masses along the two routes, and the variability of the properties and flow on timescales from days to seasons. In this study we use an extensive collection of repeat hydrographic sections occupied at three locations on the Chukchi shelf, together with data from a climatology of shipboard velocity measurements, to address some of these questions. This has allowed us, for the first time, to distinguish and quantify the two flow branches on the eastern Chukchi shelf that carry Pacific-origin water from Bering Strait to Barrow Canyon.

2. Data and methods

2.1. Hydrographic data from the Distributed Biological Observatory and Arctic Observing Network

The Distributed Biological Observatory (DBO) is a community-based program to document and understand changes to the Pacific Arctic ecosystem as a result of the changing climate. A set of key biological hotspots were identified, extending from the northern Bering Sea to the Beaufort Sea, which have been sampled repeatedly by international researchers since 2010 (Moore and Grebmeier, 2018). Most of the measurements have been done by ships of opportunity. The idea is that all of the research vessels entering the Pacific Arctic travel through Bering Strait and hence pass close to many of the DBO locations. Therefore, depending on time, interest, and resources, the ships can stop at one or more of the locations and collect measurements of the water column and benthos. The measurements range from conductivity-temperature-depth (CTD) casts to a full suite of biological and chemical sampling via water collection, net tows, and bottom grabs/cores. The aim is to make the data available to the public as soon as possible, and, in this way, build a climate record of ecosystem health and the underlying factors influencing it.

Certain DBO sites have been occupied more frequently than others. In this study we use the CTD data from the DBO3 line, which stems from Pt. Hope to the southwest, and the DBO5 line across Barrow Canyon (Fig. 2a). These two locations have the most occupations of the DBO sites, hence providing a sizable collection of repeat vertical sections. In addition, we consider occupations of the Bering Strait section. While this is not formally a DBO location, as mentioned above it is part of the Arctic Observing Network (AON; Fig. 2a). Not all of the vertical sections used in the study were done during the DBO time period; there were occupations of the Bering Strait line as early as 2000 and occupations of the DBO3 line as early as 2002. Accordingly, the time period of our study is 2000–2020, during which there were 32 occupations of the Bering Strait line (hereafter referred to as the BS line), 55 occupations of the DBO3 line, and 45 occupations of the DBO5 line. Two of the DBO3 occupations were done using a glider, while the remaining sections were shipboard occupations. Supplementary Table 1 lists the pertinent information for all of the sections.

The distribution of occupations by year and month is shown in Fig. 2b and 2c, respectively. Not surprisingly, most of the sections were done during July-September. The increase in the number of occupations coinciding with the start of the DBO program (2010) is evident. All of the sections were occupied using a Sea-Bird 911 + CTD with dual temperature and conductivity sensors, except for the two glider crossings which used a Sea-Bird Pumped Glider Payload CTD, and the three sections occupied by the R/V *Annika Marie* which used a Sea-Bird 19 + CTD. The calibration, data processing, and QA/QC were carried out according to each institution's procedures. Laboratory calibrations were generally done prior to and following each field season. The accuracy of the temperature measurements is +/-0.001 °C. For the temperature ranges observed on the Chukchi shelf, CTD temperature and conductivity sensors produce salinity data with an initial accuracy of +/-0.004 (practical salinity) with a maximum anticipated drift of +/- 0.05 for a one-year deployment according to the manufacturer. This is not a problem in light of the large range in salinity (23–34.5) encountered on the Chukchi shelf in the collective dataset. For this reason, calibration of the conductivity sensors using in-situ salinity bottle data was generally not done.

At each location a standard line was defined (Fig. 2a), and for each given section the stations were projected onto this line. Following this we used Laplacian-Spline interpolation to construct vertical sections of potential temperature (referenced to the surface, hereafter referred to as temperature), practical salinity (hereafter referred to as salinity), and potential density (referenced to the surface, hereafter referred to as density). During the gridding process some additional quality control was performed. This included removing erroneous near-surface values, interpolating over density inversions, and omitting near-repeat stations. The horizontal/vertical grid spacing of the gridded sections is 2.5 km / 2.5 m for BS, 10 km / 2.5 m for DBO3, and 2.5 km / 5 m for DBO5. Not all of the sections had complete coverage, and regions of missing data were filled in with NaNs. The bathymetry along the three standard lines was obtained using sound speed-corrected echosounder data from a ship, also projected onto the line.

2.2. Shipboard velocity data

We use velocity data from a recently compiled climatology of shipboard acoustic Doppler current profiler (SADCP) measurements for the Chukchi Sea, known as ChukSA (Bahr et al., 2023). The climatology contains data from 52 cruises over the time period 2002–2021. The space/time coverage of ChukSA is shown in Fig. 3. As with the hydrographic data, most of the measurements were collected during the months July-September. The profile data were subject to rigorous quality control, which included transducer calibration and orientation checks followed by subsequent adjustments, as well as visual profile editing. Standard SADCP issues included isolated cases of CTD package interference with the acoustic beams as well as apparently good velocity

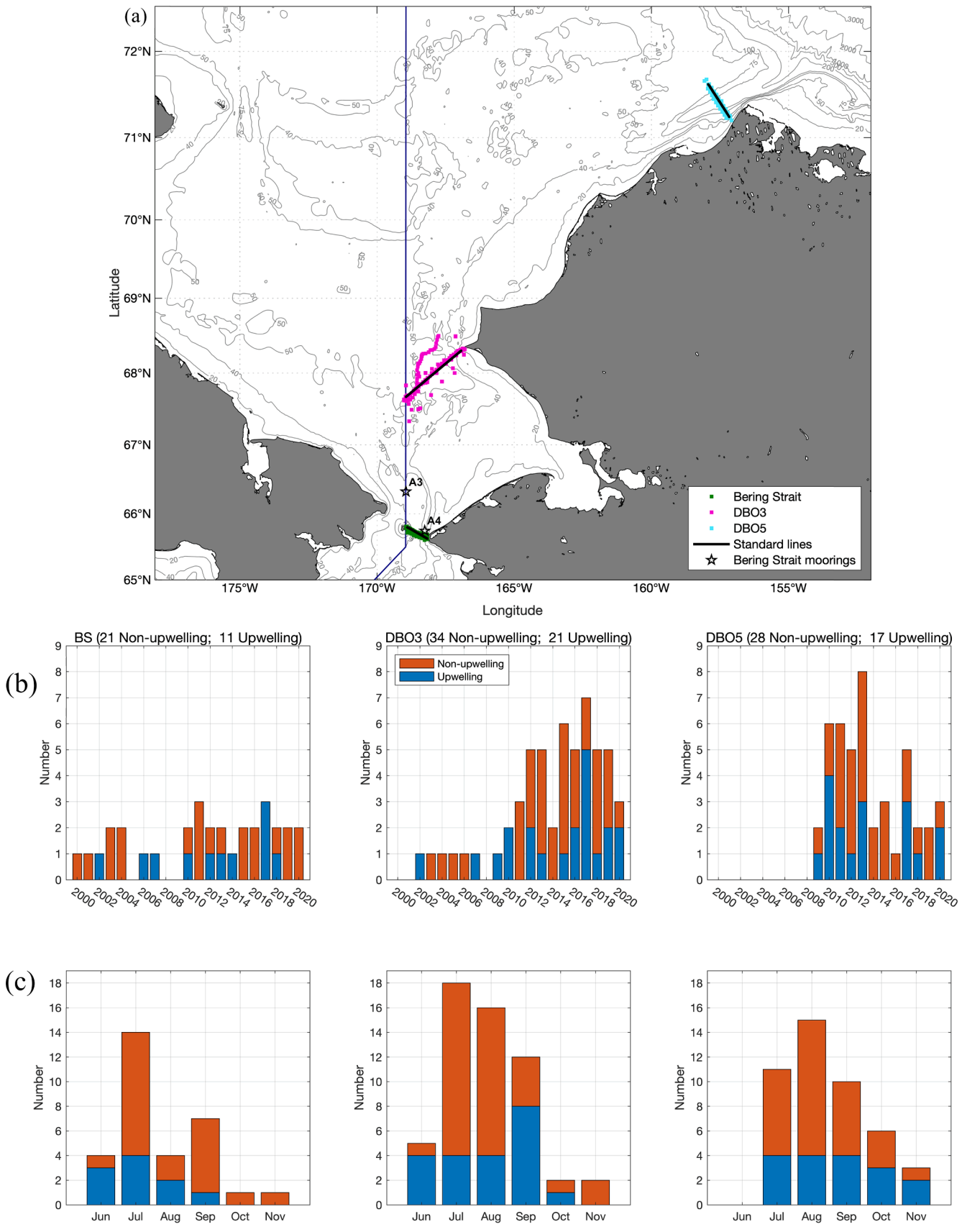

Fig. 2. (a) Occupations of the hydrographic sections at the three sites. The standard lines are shown (black lines), and the two Bering Strait moorings used in the study are labeled. The bathymetry (in meters) is from IBCAO v3. The blue line indicates the US/Russian convention line. (b) Temporal distribution of the occupations by year and (c) by month, distinguished by non-upwelling (red) and upwelling (blue) conditions (see Section 2.6 for delineation of upwelling status).

estimates from depths below the bottom when operating in shallow water. The ChukSA climatology includes data from ice capable vessels whose smooth hulls can exacerbate bubble issues. This tends to occur during rough conditions in ice-infested waters, which leads to "underway bias" – a typically surface-trapped erroneous increase in velocity in the direction of the ship's motion. Bad data can also occur when parts of broken ice floes get pushed under the hull which interferes with, or even fully blocks, the acoustic beams. After the quality control was finished for each dataset in the climatology, the barotropic tidal signal was removed from the velocity profiles using the Oregon State University tidal model (https://volkov.oce.orst.edu/tides; Padman and Erofeeva, 2004). The overall estimated velocity error is taken to be 2 cm/s (Pickart et al., 2016).

The ChukSA velocity data were used to construct vertical sections of mean absolute geostrophic velocity as follows. A swath of SADCP data corresponding to the BS line (10 km swath), the DBO3 line (10 km swath), and the DBO5 line (6 km swath) was extracted, and mean vertical sections of alongstream velocity were constructed in analogous fashion to the hydrographic sections, with a grid spacing of 2.5 km / 5 m for DBO3 and DBO5, and 5 km / 5 m for BS. These sections were then used to reference the mean thermal wind sections (after interpolating the velocity sections to the same grid as the hydrographic fields) following the method described in Pickart et al. (2016). Transport calculations were done using the mean gridded absolute geostrophic velocity sections, and uncertainty estimates were based on the conservative assumption of uncorrelated errors across the section.

2.3. Historical hydrographic data

To construct a mean lateral map of near-surface density over the Chukchi shelf, we use the historical hydrographic dataset invoked by Lin et al. (2021). This is a combination of multiple data sources, the two predominant ones being the Unified Database for Arctic and Subarctic Hydrography (UDASH) covering the period 1980–2015 (Behrendt et al., 2018), and the World Ocean Database 2018 (WOD18) spanning 1849–2020. To enhance the data coverage, we included a composite dataset of hydrographic observations in the Chukchi Sea spanning 1922–2019 (Danielson et al., 2020), along with recent shipboard measurements from the Arctic Data Center that have not yet been added to the datasets above. We consider the time period of July-September 1970–2020. The near-surface level is taken to be the average over the top 10 m of the water column, since many of the profiles did not have values shallower than 5 m.

2.4. Wind data

We use the ERA5 10-m reanalysis wind data from the European Centre for Medium-Range Weather Forecasts (ECMWF, Hersbach et al., 2018). The spatial resolution of this product is 1/4° and the time resolution is 1 h. Past studies have shown good agreement between the ERA5 winds on the northeast Chukchi shelf and those measured at the meteorological station in Utqiaġvik, AK (e.g., Lin et al., 2021).

2.5. Ice concentration data

To help in the interpretation of some of the results, we use satellite ice concentration data from the Advanced Microwave Scanning Radiometer for EOS (AMSR-E) for the years prior to 2012, and the Advanced Microwave Scanning Radiometer 2 (AMSR2) for 2012 onward. Both of these are daily products provided by the Remote Sensing of Sea Ice Research Group at the University of Bremen, with a spatial resolution of 3.125 km in the domain of interest.

2.6. Determining upwelling vs. non-upwelling conditions

The flow in Bering Strait and across the Chukchi shelf is sensitive to both local winds as well as remote winds over the Bering shelf (Danielson et al., 2014). Under enhanced local northeasterly winds, the flow in Barrow Canyon reverses to the south and upwelling commences (e.g., Mountain et al., 1976; Danielson et al., 2017; Weingartner et al., 2017; Pisareva et al., 2019; Lin et al., 2019). The same is true for Bering Strait when the northerly winds intensify (e.g., Aagaard et al., 1985; Pisareva et al., 2015; Woodgate, 2018). Not surprisingly, a good number of the DBO and BS occupations occurred under wind-forced conditions when upwelling was active (Fig. 2). The present study focuses on the non-upwelling state of the circulation, or what might be termed the background state. As such, it was necessary to devise a method for identifying the upwelling realizations in order to remove them from our collection of sections.

A characteristic signature of coastal upwelling along the eastern

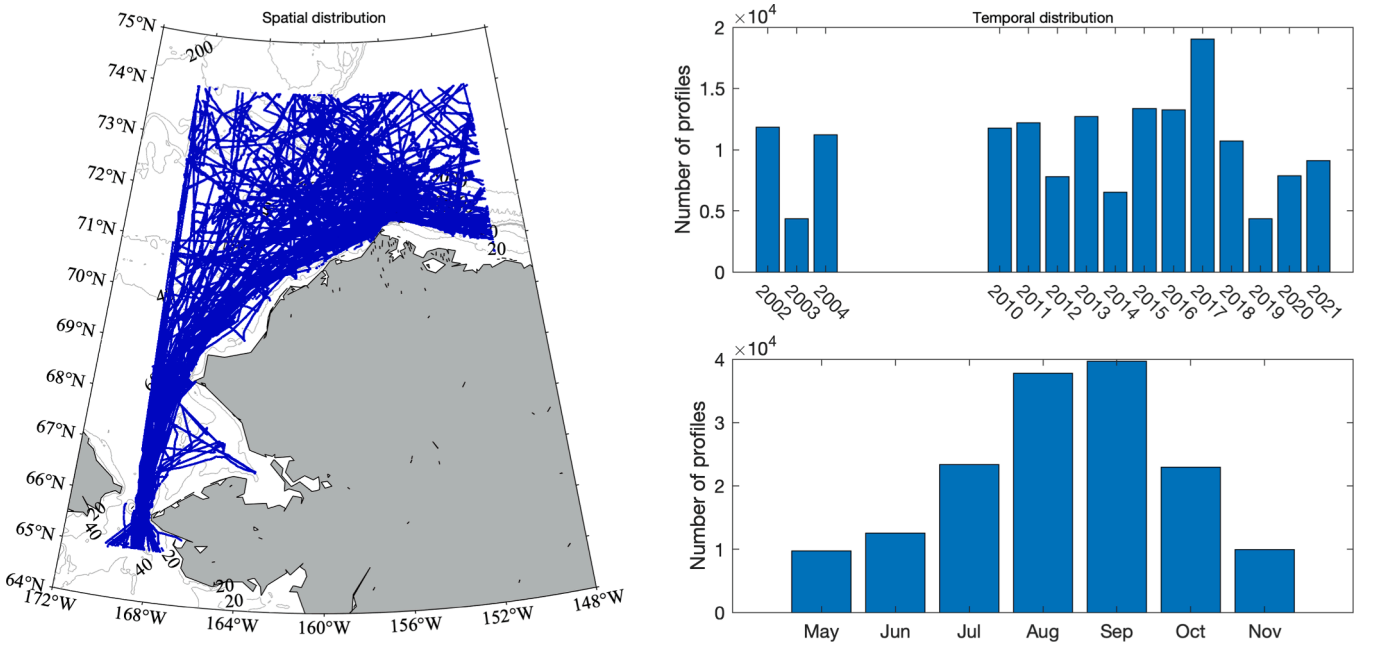

Fig. 3. The ChukSA climatology of shipboard ADCP data. (left) Spatial coverage. (right) Temporal coverage by year and month.

boundary of the Chukchi Sea is the presence of anomalously salty water banked up against the slope (e.g., Pickart et al., 2019). Accordingly, at each site we defined a polygon at the eastern end of the transect, where the bottom slope is steepest, that extended 10 m above the bottom (Supplementary Fig. 1). For each occupation we then computed the average salinity within the polygon and took the difference between that value and the mean of all the transects at the site, referred to as S_{anom}. When S_{anom} exceeded a certain value, the section was deemed to be under the influence of upwelling. For DBO5 the criterion was taken to be $S_{anom} > 0$, for DBO3 $S_{anom} > 0.1$, and for BS $S_{anom} > 0.5$. These values were determined by inspection of the hydrographic signals at each location, which were quite obvious, and the results were insensitive to small changes in the values. The different criteria reflect differences in the near-bottom lateral salinity gradients at each site. Supplementary Fig. 1 shows the mean vertical sections of salinity for the non-upwelling state vs upwelling state at BS. In the latter, not only is salty water banked-up along the bottom, but the near-surface freshwater layer extends farther offshore. This is the expected signature of the secondary circulation during upwelling. Overall, 37% of the sections were occupied during upwelling conditions. The number of realizations that sampled the background state was 21(out of 32), 34 (out of 55), and 28 (out of 45) for BS, DBO3, and DBO5, respectively (Fig. 2b). This subset of sections is used throughout the present study except where indicated. Future work will investigate the upwelling realizations.

It was also necessary to distinguish the upwelling vs. non-upwelling states associated with the ChukSA velocity data. To do this we relied on mooring data near each of the standard lines (see Supplementary Fig. 2 and Supplementary Table 2): for BS, mooring A4; for DBO3, mooring MC6; and for DBO5, mooring BC2. At each site, the alongstream direction was taken to be the angle of the mean flow vector (depth-averaged flow at BS and DBO5, and near-bottom flow at DBO3 since the MC6 mooring had only a single point current meter). Based on this, it was determined that, for DBO3 and DBO5, upwelling conditions corresponded to negative alongstream velocities, whereas for BS, upwelling corresponded to alongstream velocities < 25 cm/s (or negative). The reason for the different criterion at BS is that it takes stronger winds to reverse the flow there due to the large northward velocities associated with the narrow constriction of the strait.

As noted in Section 2.2, we extracted a swath of the ChukSA velocity data corresponding to the three standard lines (see Supplementary Fig. 2). For DBO5, upwelling was identified when the alongstream SADCP velocity was negative within the coastal region (within 30 km of the eastern end of the section), where we also included data collected within $\pm$ 24 hrs on the offshore part of the section. The same procedure was done for DBO3, where the coastal region was defined as within 60 km from the eastern end of the section. For BS, the entire section was taken to be in the coastal region which was considered upwelling influenced when the alongstream SADCP velocity was < 25 cm/s. Supplementary Fig. 2 shows the space/time ChukSA coverage for the upwelling and non-upwelling conditions at the three sites. In this study we used the mean non-upwelling SADCP sections to reference the mean non-upwelling thermal wind sections, following the procedure outlined in Section 2.2.

2.7. Defining the Alaskan Coastal current hydrographic front

In order to characterize the water being transported by the Alaskan Coastal Current, we devised an objective procedure for determining the Alaskan Coastal Water density front for each realization at the three different sites. For each section, the near-surface lateral density gradient, $\partial\rho_s/\partial x$, was calculated, and the density corresponding to the maximum value of $\partial\rho_s/\partial x$ was taken as the center isopycnal of the front. An example is shown in Supplementary Fig. 3, applied to the July 2003 occupation of the BS line. A pronounced maximum in $\partial\rho_s/\partial x$ (computed at 2.5 m depth) is evident near $x = 28$ km, which corresponds to a density of 23.86 kg/m^3. This isopycnal was then identified as the center of the front for this realization, and the Alaskan Coastal Water taken to be the water inshore of this front (Supplementary Fig. 3). In some cases there was more than one peak in $\partial\rho_s/\partial x$, or a slightly deeper depth had to be chosen to compute the density gradient, or there was a detached lens of Alaskan Coastal Water offshore. Such instances were easy to negotiate, and, for nearly all of the realizations, it was immediately obvious where the front was.

2.8. Empirical orthogonal function analysis

To investigate the mesoscale to seasonal variability at the three sites, we carry out an empirical orthogonal function (EOF) analysis. This is possible because all of the sections at each site are on an identical grid. The eigenfunctions (spatial patterns) and eigenvalues are computed for the co-variance matrix of a given variable (temperature, salinity, and density). To better interpret the physical meaning of the modes, we compute "minimum" and "maximum" states. This is done by multiplying plus/minus a given percent of the principal component (PC) timeseries by the spatial structure of the mode, then adding this to the mean vertical section. The percent chosen typically corresponds to one standard deviation (we note when this is not the case).

2.9. One-dimensional mixing model

To help investigate the modification of the water progressing northward across the Chukchi shelf, we use the one-dimensional mixing model of Price et al. (1986), hereafter referred to as the PWP model. The model is applied in an advective framework following both the Alaskan Coastal Current and Central Channel pathway. For initial conditions we use hydrographic profiles from Bering Strait. The profiles are forced by the surface heat flux and windstress from ERA5 along the pathways. This method was successfully used to isolate the impact of air-sea forcing on the along-pathway transformation of water masses in the Nordic Seas boundary current system (see the methods section of Huang et al. 2023).

3. Results

3.1. Mean background state

Following previous studies, we consider two different types of Pacific-origin summer water and two different types of Pacific-origin winter water (e.g., Li et al., 2019): Alaskan Coastal Water (ACW) originating from runoff from the Alaskan land mass; Bering Summer Water (BSW) which is a combination or mixture of Anadyr water and central Bering shelf water (Coachman et al., 1975; Danielson et al. 2020); Newly Ventilated Winter Water (NVWW), which is formed via brine-driven convective overturning during the winter and early spring; and Remnant Winter Water (RWW) which is NVWW that has been warmed via solar heating and/or mixing with summer waters (Gong and Pickart, 2016). Other water types found on the Chukchi shelf include sea-ice melt water and meteoric water, which we do not distinguish and consider as a single classification referred to as MWM, and Atlantic Water (AW) which resides near the bottom at the mouth of Barrow Canyon and can occasionally be advected onto the northern Chukchi shelf via upwelling (e.g., Ladd et al., 2016; Hirano et al., 2016; Pisareva et al., 2019; Li et al., 2022).

The definitions of the water masses are listed in Table 1 and shown graphically in Fig. 4, which shows the percent occurrence in temperature/salinity (θ/S) space of the different water masses for all of the non-upwelling realizations. We split the presentation into BS + DBO3 (Fig. 4a) and DBO5 (Fig. 4b), since the DBO5 line is so far to the north (Fig. 2a). At the southern two transects the dominant water type is BSW with very little RWW and no NVWW. By contrast, the most commonly occurring water types at DBO5 are the two winter waters, RWW and NVWW. As discussed in Pickart et al. (2019), during late summer the Pacific-origin winter water is still draining from Barrow Canyon, having

Table 1
Temperature-salinity definitions of the water masses considered in the study.

Alaskan Coastal Water (ACW)	$T > 3$ °C, S = 29.5–31.5
Bering Summer Water (BSW)	T = 0–3 °C, S = 30–33.64, and $T > 3$ °C, S = 31.5–33.64
Remnant Winter Water (RWW)	T = −1.6–0 °C, S = 31.5–33.64, and T = −1.6 – −1.26 °C S > 33.64
Newly Ventilated Winter Water (NVWW)	$T < -1.6$ °C, S > 31.5
Melt Water / Meteoric Water (MWM)	$T < 0$ °C, S = 30–31.5, $T < 3$ °C and S = 29.5–30, and S < 29.5
Atlantic Water (AW)	$T > -1.26$ °C, S > 33.64

taken the longer Central Channel pathway which brings the water around the northern side of Hanna Shoal (Fig. 1; see also Pickart et al., 2016; Shroyer and Pickart, 2019). Another marked difference between the two panels is in regard to the MWM, which is relatively warm at BS and DBO3 and relatively cold at DBO5. This likely reflects sea-ice melt; since melt-back occurs later on the northern Chukchi shelf, the melt water will be colder there during summer. Finally, there is a very small amount of AW present at the DBO5 line. This is found at the bottom of the section.

It is important to note that these water mass boundaries are meant only as guidelines for general context. For example, there is every reason to believe that the boundaries change somewhat from year to year (Coachman et al., 1975). Indeed, when using our objective approach in Section 2.6 to define the hydrographic front of the Alaskan Coastal Current, in some realizations the water within the current was outside the θ/S range used in previous studies for ACW (e.g., Pickart et al., 2019). As such, we adjusted our ACW definition accordingly. We also note that these water mass classifications do not necessarily correspond to mode waters, although seasonally certain classes will contain volumetrically more water (see below). Nonetheless, it is useful to consider such classifications; for example, the ACW typically resides in the Alaskan Coastal Current, while in summer the Central Channel pathway advects mainly BSW.

The mean non-upwelling vertical sections of hydrographic properties and absolute geostrophic velocity for the three lines are shown in Fig. 5. At each location there is a warm, fresh wedge of water on the eastern end of the section, which is the signature of the ACW. This wedge is notably less warm and fresh at DBO5. Another unique aspect of DBO5 is that the isopycnals of the ACW do not outcrop as they do at the two southern locations; rather, there is a fresh surface layer across the entire DBO5 transect. The nature of this feature is addressed below in Section 3.3. The coldest and saltiest water resides at depth on the western ends of each section. As noted above, in Barrow Canyon this is Pacific-origin winter water, while at the two southern transects it is relatively cold and salty BSW. At all three sites the pycnocline is shallower than 20 m on the western end of the section, and the isopycnals slope downward into deeper depths progressing towards the eastern end of the section. The mean absolute geostrophic velocities are northward and surface-intensified at each transect, with the strongest flow at BS.

3.1.1. *Volume transports*

At each of the transects there is enhanced northward flow on the eastern side (Fig. 5g-i). This is the kinematic signature of the Alaskan Coastal Current (hereafter referred to as the ACC). Seaward of this, a second region of enhanced flow corresponds to the Central Channel branch (hereafter referred to as the CC Branch). We chose the region of minimum flow in the upper layer as the division between these two branches. The offshore edge of the CC Branch was chosen as follows: at BS this was taken to be the western end of the section (i.e., Little Diomede Island); at DBO3 this was chosen to exclude the region of enhanced northward flow at the western edge of the section (which is assumed to have originated from the Russian side of Bering Strait); and for DBO5 this was taken to be where the northward flow approaches zero. Remarkably, based on these straightforward choices, the volume transports of each branch are statistically the same at all three locations – i.e., mass is balanced. To our knowledge this is the first time that the ACC and CC Branch have been unambiguously resolved and their transports quantified. The individual transport values are listed in Table 2. Averaged over the three locations, the transport of the ACC is 0.34 ± 0.04 Sv and that of the CC Branch is 0.86 ± 0.11 Sv, totaling 1.20 ± 0.13 Sv. Keep in mind that these values correspond predominantly to the months of July-September (see Fig. 2c).

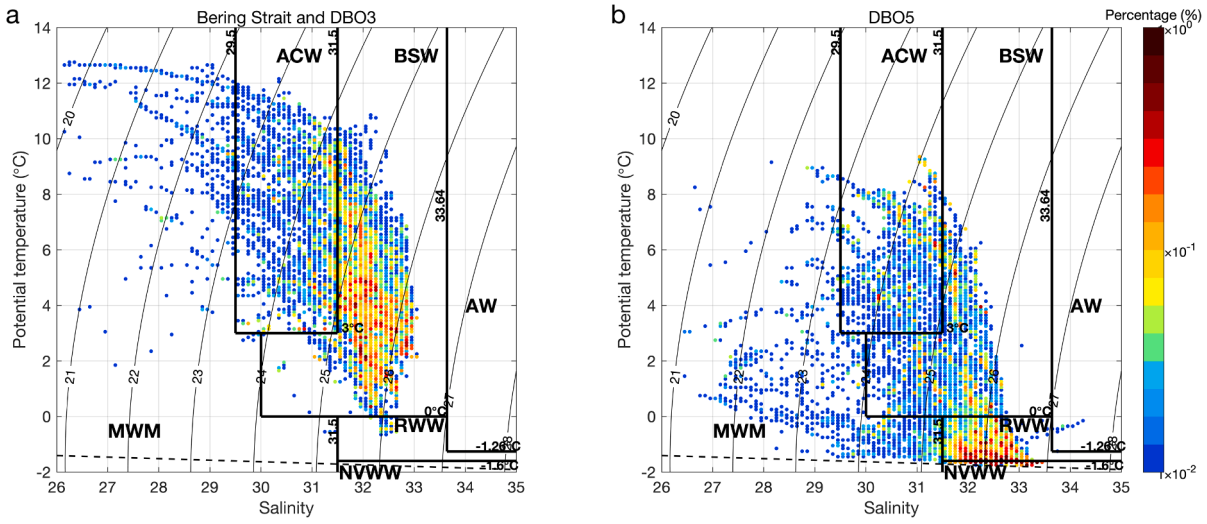

Fig. 4. Percent occurrence temperature/salinity diagram for (a) the non-upwelling BS + DBO3 sections, and (b) the non-upwelling DBO5 sections. The color indicates the percent occurrence within a given bin of 0.1 °C in temperature by 0.01 in salinity. Contours are density (kg m^{-3}). The water mass boundaries are indicated by the thick black lines. ACW = Alaskan Coastal Water; BSW = Bering Summer Water; RWW = Remnant Winter Water; NVWW = Newly Ventilated Winter Water; MWM = sea-ice melt water / meteoric water; AW = Atlantic Water.

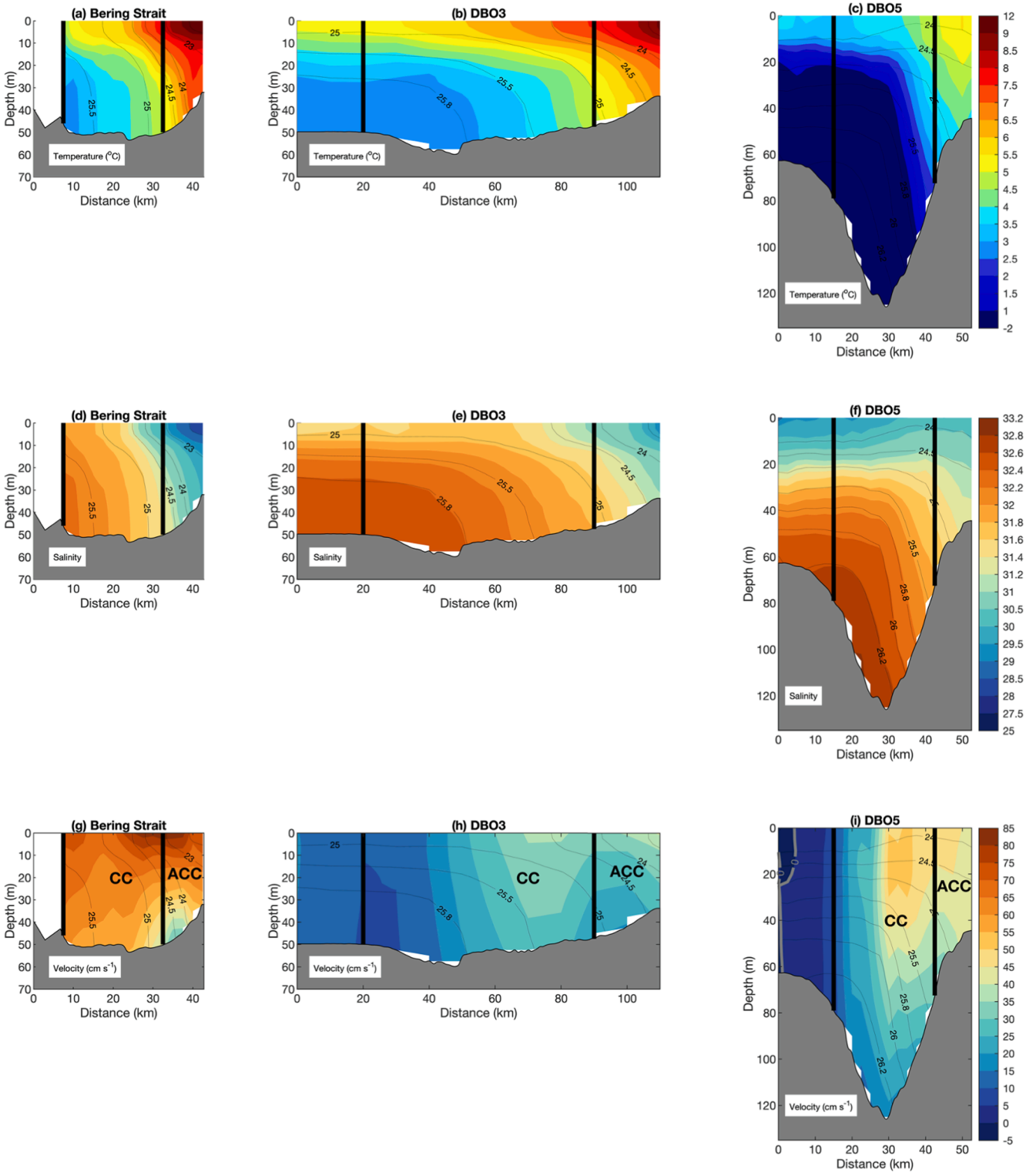

Fig. 5. Mean non-upwelling vertical sections at the three sites. The top row is temperature, the middle row is salinity, and the bottom row is absolute geostrophic velocity. The thick black lines delineate the Alaskan Coastal Current (ACC) and Central Channel (CC) flow branches. The left column is BS, the middle column is DBO3, and the right column is DBO5. The contours are the mean isopycnals (kg m^{-3}). The bottom topography is from sound speed-corrected shipboard echosounder data.

It is of interest to compare the transports calculated here to the transport through Bering Strait calculated using the AON mooring data. Since the majority of our transect data were collected after 2010, we use the mooring data from 2010 to 2021 (Woodgate et al., 2015; Woodgate, 2018; Woodgate and Peralta-Ferriz, 2021). We multiplied the depth-mean velocity at mooring A3 (see Fig. 2a) by the cross-sectional area of the strait (the US side plus the Russian side), excluding the area of the ACC, to get the full transport minus the ACC. To get the ACC contribution, we multiplied the depth-mean velocity at mooring A4 by the estimated cross-sectional area of the ACC according to Fig. 5g (0.58 km^2).

Table 2
Volume transport (Sv) of the different flow branches calculated from the mean absolute geostrophic velocity sections at the three sites for non-upwelling conditions. The uncertainty at each site is from the estimated measurement error, and the uncertainty in the overall mean also reflects the spread in values at each site.

	ACC	CC	Total
BS	0.34 ± 0.01	0.87 ± 0.03	1.21 ± 0.04
DBO3	0.37 ± 0.03	0.81 ± 0.08	1.18 ± 0.10
DBO5	0.32 ± 0.02	0.88 ± 0.06	1.20 ± 0.08
Overall Mean	**0.34 ± 0.04**	**0.86 ± 0.11**	**1.20 ± 0.13**

The monthly mean timeseries of the total transport and that of the ACC are shown in Fig. 6. The full transport peaks near 1.6 Sv during May-July, while the ACC transport peaks near 0.4 Sv in July.

We note that the mooring values include both the non-upwelling and upwelling periods. Hence, to do a fair comparison, we computed the mean absolute geostrophic velocity section at BS using all of the hydrographic realizations together with all of the SADCP data, then computed the volume transport across the full BS section as well as that of the ACC (using the same division point as in Fig. 5g to delineate the ACC). The resulting transports are marked by the large open stars in Fig. 6. Since the majority of the BS hydrographic sections were occupied in the months of July, August, and September, we subsequently computed the mean mooring value for these three months, weighted by the number of hydrographic realizations in each month. These transports are marked in Fig. 6 by the large filled stars. Comparing these to the open stars, one sees that the ACC transports are very similar (indistinguishable within the error bars); this is to be expected because the ACC resides on the US side of the strait. By contrast, our full transport (1.08 ± 0.04 Sv) is less than the value using the moorings (1.44 ± 0.11 Sv), which is also expected since we do not measure the transport through the Russian side of the strait. Our result implies that, during the months of July-September, approximately 75% of the Bering Strait inflow passes through the US side of the strait. This is near the high end of the summertime range deduced from the three long-term mooring arrays on the Chukchi shelf (see the Introduction).

3.2. Seasonality

We now investigate the seasonality of the water being advected by the ACC and CC Branch at the three sites. As explained in Section 2.6, we define the ACC water mass as that inshore of the central isopycnal of the ACC hydrographic front. For the CC Branch it is not obvious how to identify an analogous front, so we use geographical limits. For BS and DBO5 we use the same bounds as indicated in Fig. 5g and 5i, respectively. For DBO3, the offshore extent for the CC Branch water mass is taken to be slightly more inshore than what was used for the transport, 40 km versus 20 km. The reason for this is that, as noted above, the offshore part of this line appears to be influenced by water from the Russian side of Bering Strait, in particular, the Anadyr Water. This is consistent with the high levels of water column productivity and benthic biomass measured in this region (Grebmeier et al., 2015; 2018). Inspection of the DBO3 sections indicated that a distinct water mass is often found there (which occasionally can be present to a small degree in the CC flow path), and we wanted to avoid aliasing this hydrographic signature into the CC water mass. Investigation of the Anadyr-like water at DBO3 will be the subject of future study.

For each realization at each site, we averaged the water properties shoreward of the ACC front and those within the CC Branch as defined

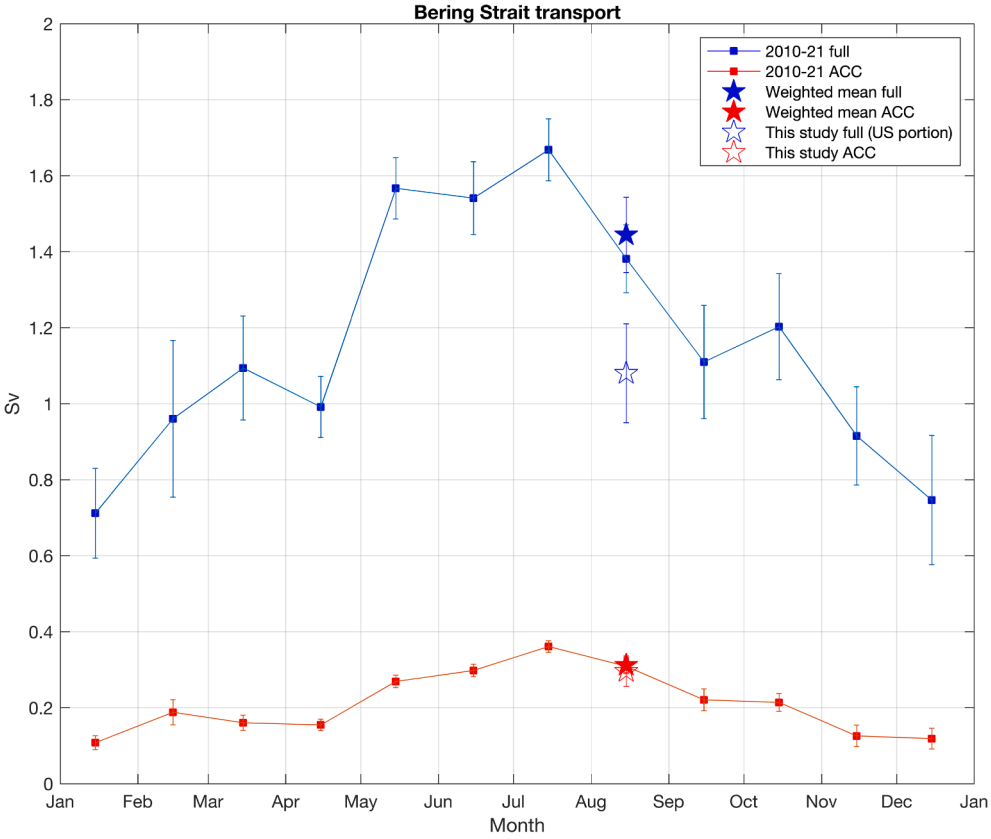

Fig. 6. Comparison of transports from this study to that calculated using the Bering Strait moorings (see the legend). The small blue and red filled squares are the monthly mean values for the full transport and the ACC portion, respectively, from the moorings. The large filled stars are the corresponding weighted mean values for Jul-Sep as described in the text. The large open stars are the mean values calculated in this study for the US portion of the strait (blue) and the ACC (red). Standard errors are included.

above. Occasionally some of the ACC water extended into the geographical domain of the CC Branch, including a few instances where there was a detached lens of the water located well offshore of the ACC. These regions were excluded when computing the CC Branch averages. Fig. 7 shows the ACC water mass characteristics at BS as a function of year day. While there is significant scatter, a clear seasonal pattern is evident: the ACC is warmest, freshest, and lightest in late summer. While there are not enough ChukSA velocity data to construct absolute geostrophic velocity sections for each realization, we can compute the baroclinic velocity (relative to the bottom) for each section. This reveals that, in addition to being warmest and freshest, the baroclinic flow of the ACC is strongest in September (keeping in mind that the strongest full transport of the ACC occurs in July according to the Bering Strait mooring data; see Fig. 6).

Another way to address the seasonality at BS is via an EOF calculation (see Section 2.7). We performed the analysis separately on the temperature, salinity, and density sections. The EOF mode 1, which explained between 50 and 70% of the variance for the three variables, reflects the seasonal variation. The vertical structure and PC timeseries for temperature and salinity are shown in Fig. 8a-d. These are scaled so that the contours in Fig. 8a and 8c denote the maximum dimensional amplitude of the mode for temperature and salinity, respectively. This reveals that seasonal warming occurs across the entire section. Perhaps unexpectedly, the maximum warming occurs outside the core of the ACC in the lower part of the water column, extending to the middle of the section. By contrast, the freshening occurs mainly on the eastern side of the section and is surface-intensified, with the maximum signal within the ACC. To visualize the impact of this modal structure, we multiplied plus/minus one standard deviation of the PC timeseries by the spatial structure and added it back into the mean (Fig. 8e-h). This clearly shows the nature and extent of the seasonal change in the ACC from early-July to mid-September (we note that the basic hydrographic vertical structure remains similar to the mean vertical structure; Fig. 5a, 5d). While these trends are not surprising, Figs. 7 and 8 represent the first full water column quantification of this. Averaged over the region inshore of the frontal isopycnal of the ACC, the amplitude of the seasonal change is 3.6 °C in temperature and 2.6 in salinity.

Farther to the north, the seasonality is less pronounced. At DBO3 there is no discernable seasonal signal in salinity for either the ACC or the CC Branch, and, at DBO5, this is true for both salinity and temperature. In these cases, the variability in water properties is mainly dominated by other processes – this is investigated below in Sections 3.3 and 3.4. Fig. 9 shows the variation in temperature at BS and DBO3 for the two flow branches (again, it is the average for each realization at each site). While there is significant scatter in each case, a seasonal signal is evident. As was true for the ACC in BS, the temperature of the CC Branch in BS peaks in September (compare Fig. 9a,b). While the temperatures are considerably colder in the CC Branch, the amplitude of the warming is comparable as seen in the EOF vertical structure of Fig. 8a. Farther north at DBO3 the warmest temperatures for both the ACC and CC Branch are generally found in August, compared to September for BS. This is likely due to the fact that, staring in early-

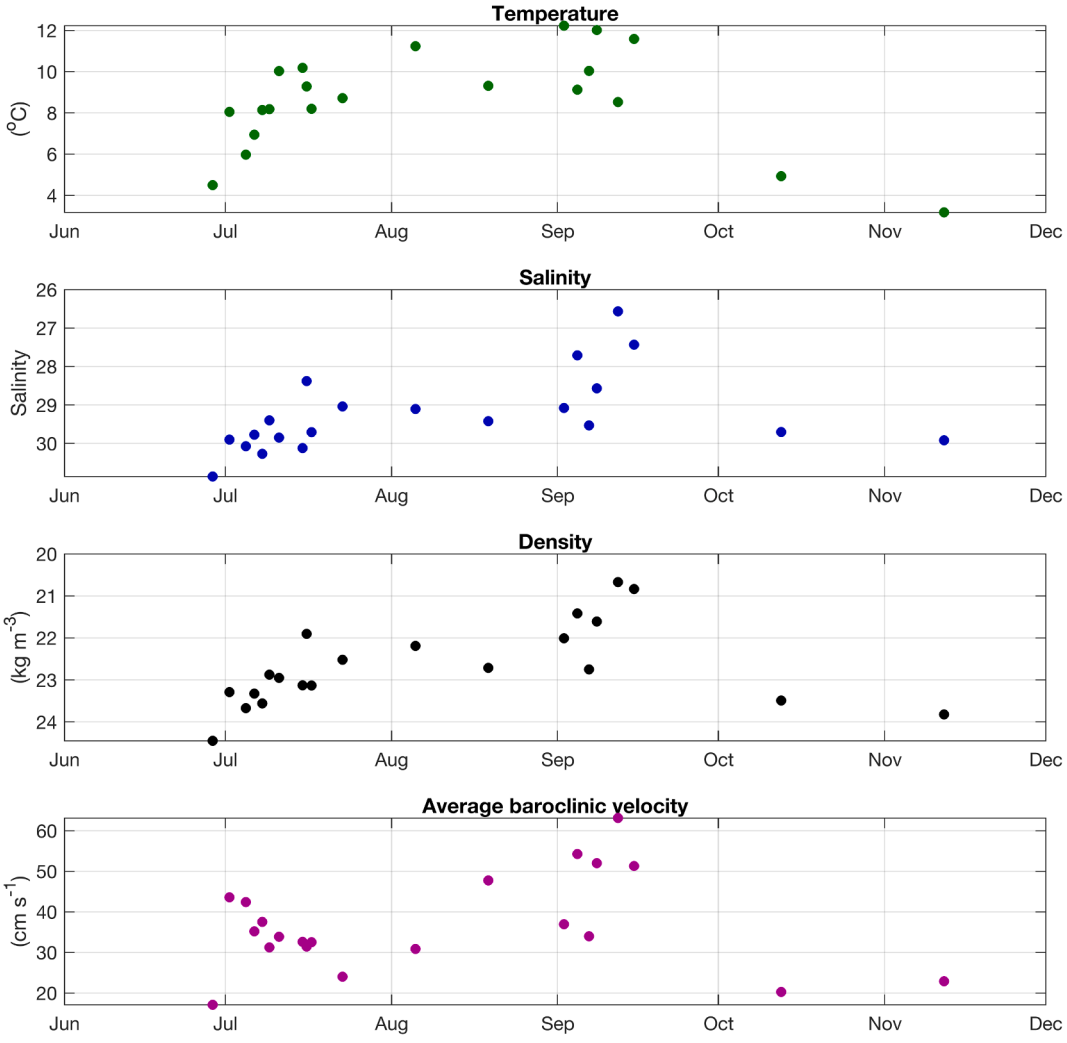

Fig. 7. Properties of the ACC at Bering Strait as a function of year day. The circles are averages inshore of the frontal isopycnal for each occupation (see text).

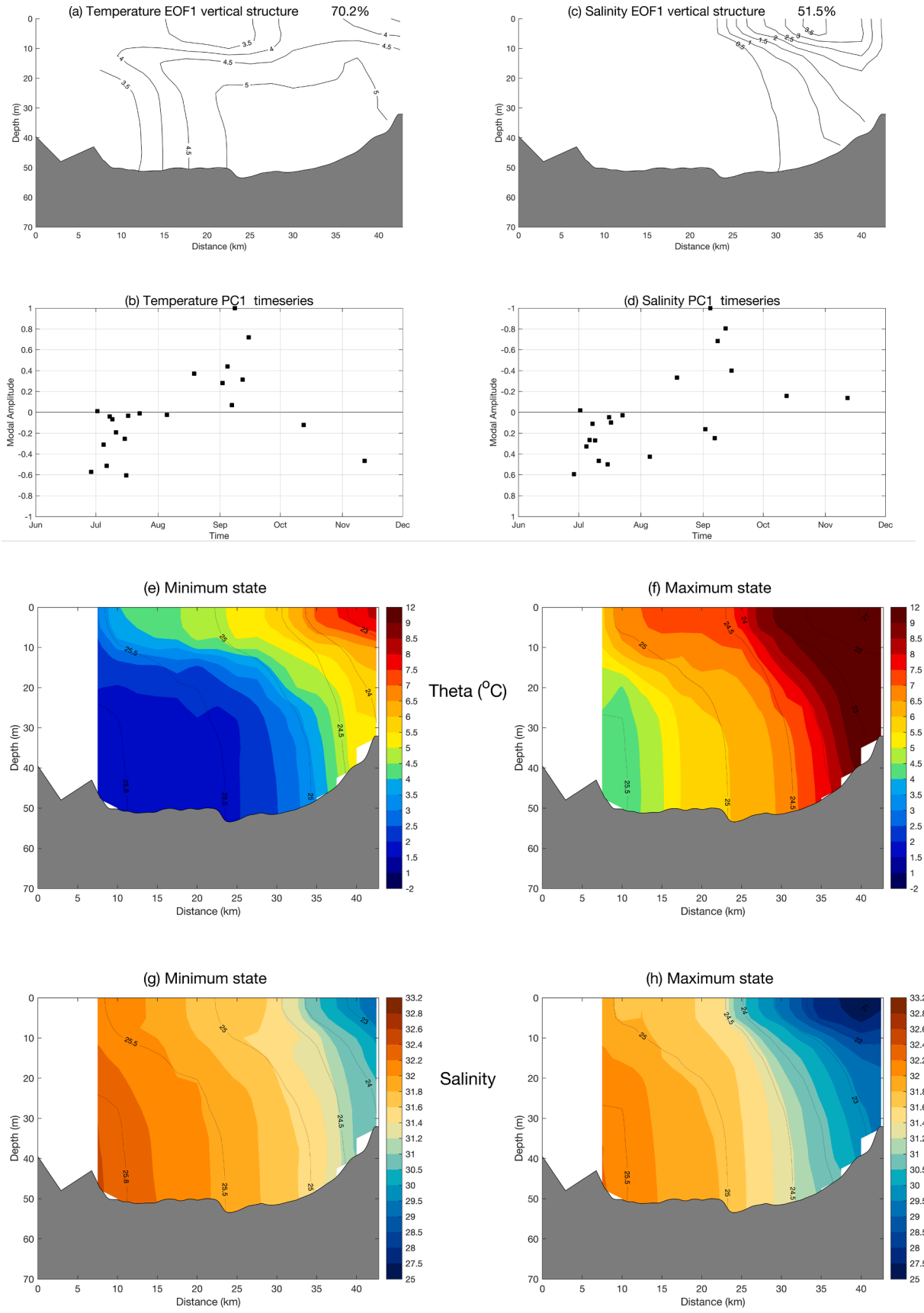

Fig. 8. EOF mode 1 (EOF1) for Bering Strait. (a) Vertical structure for temperature, where the contours represent the maximum dimensional amplitude of the mode. (b) Principal component (PC1) timeseries for temperature as a function of year day. (c) Same as (a) for salinity. (d) Same as (b) for salinity. The percent variance explained by each mode is indicated. (e) Minimum and (f) maximum states of EOF 1 for temperature. (g) Same as (e) for salinity. (h) Same as (f) for salinity. The contours are density (kg m^{-3}). The bottom topography is from sound speed-corrected shipboard echosounder data.

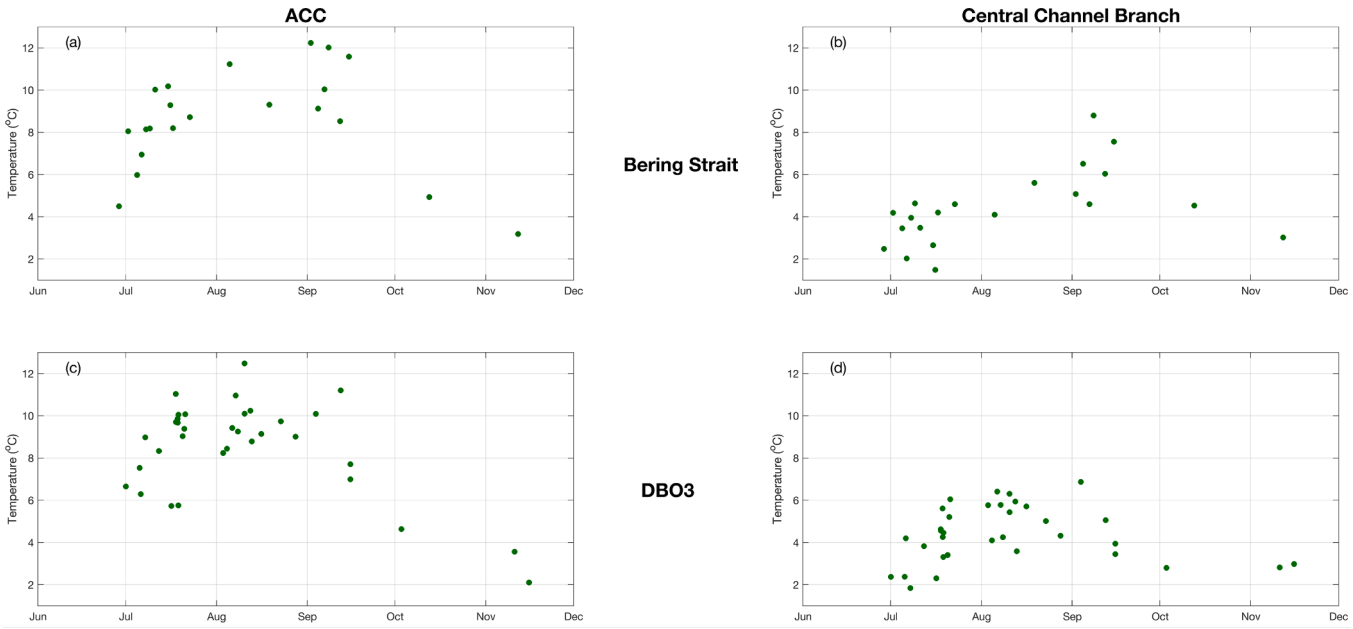

Fig. 9. Average temperatures of the ACC and CC Branch at Bering Strait and DBO3 as a function of year day. Note that panel (a) is the same as the top panel in Fig. 7.

September, the air-sea heat flux changes sign in the Chukchi Sea such that the atmosphere begins to cool the ocean, with the flux being considerably larger north of Bering Strait (Fig. 17, which is discussed in more detail below in Section 3.5).

3.3. Dominant variability at DBO5

As noted above, there was no identifiable seasonal signal in temperature or salinity at DBO5 for either the ACC or the CC Branch. We now describe the dominant variability in hydrographic properties at this location and investigate the underlying causes. Applying the same EOF calculation that was done above to the BS sections, except now to the DBO5 sections, reveals a dominant salinity mode that corresponds to freshening of the upper layer of the water column across the entire section, enhanced on the western side (Fig. 10)[1]. The mode explains approximately 45% of the variance. The PC1 timeseries is presented as realization #, which is simply the section number in the order in which it was processed (i.e., not a physically meaningful order). The comparable density mode (38% of the variance) has a nearly identical vertical structure and PC timeseries (not shown). What is the nature of this mode? We suspect that it is due to ice melt on the northern Chukchi shelf. To demonstrate this, we used the satellite ice concentration data to compute the net change in concentration at each grid point over the 10 days prior to the time of each occupation (the result is not sensitive to the exact choice of days). Positive values represent ice gain, while negative values indicate ice loss. Following this, we made a composite average for all of the realizations whose PC values in Fig. 10b were>0.5 times the standard deviation (5 occupations), and another one for all the realizations whose PC values were less than −0.5 times the standard deviation (8 occupations).

In the former case, which corresponds to the presence of the fresh layer across the DBO5 section, there was considerable ice loss over the northeast Chukchi shelf during the preceding 10 days – up to 20% in the vicinity of Barrow Canyon (Fig. 11a). By contrast, in the latter case there was essentially no change in ice concentration throughout the region (Fig. 11b). These differences can be understood by compositing the mean ice concentration over the 10-day period for the two cases. When the fresh layer is present, the ice concentration is approximately 10% in the vicinity of Barrow Canyon and up to 25% northwest of the canyon (Fig. 11c), suggesting that plenty of melt water should be present. When the fresh layer is absent or reduced, the entire area corresponds to open water – i.e., melt-back had already occurred over the northeast shelf (Fig. 11d) implying a diminished presence of newly formed melt water.

To shed light on the different timing of melt back, we calculated the mean 2-m air temperature over the northeast Chukchi shelf during the months of July-September for all of the ± 0.5 standard deviation realizations of PC1. In addition, we calculated the heat flux through Bering Strait for the months of June-August for these realizations. The idea is that instances of earlier meltback would correspond to greater oceanic heat flux into the Chukchi Sea and/or warmer regional air temperatures (for a diagnosis of summer surface and lateral heat fluxes in the Chukchi Sea, see Lu et al., 2020). For the earlier melt-back cases, the heat flux through Bering Strait was 26.3 ± 2.8 TW and the mean air temperature was 2.5 ± 0.4 °C, while for the later melt-back cases these values were 15.6 ± 2.5 TW and 1.5 ± 0.1 °C, respectively. Hence, both factors likely contributed to the change in melt-back and hence the presence/absence of the fresh layer across Barrow Canyon revealed by the EOF.

While the dominant signal in salinity (and density) at DBO5 appears to be related to variations in ice melt on the northeast Chukchi shelf, the dominant temperature variability is not associated with this process. In particular, the PC1 timeseries for temperature is not correlated with that for salinity, and the EOF1 vertical structure for temperature is qualitatively different than that for salinity. This is not to say that there is no temperature signal related to the ice melt. Such a signal is evident by constructing composite average vertical sections corresponding to the two groupings of occupations used above for the satellite ice concentration composites (i.e., based on the salinity PC1 timeseries). In the positive composite, the fresh surface layer is associated with significantly colder temperatures: averaged over the top 15 m of the water column and across the section, the temperature is colder by 2.6 ± 0.76 °C than in the negative composite (the salinity is fresher by 1.9 ± 0.37). Such colder water is expected where there is actively melting ice. The dominant temperature variability at DBO5, captured by the EOF1 temperature mode (55% variance explained), is associated with warming throughout the section, with a maximum signal in the ACC. At this

[1] The August 2013c section had an anomalously fresh layer at the surface which dominated the original EOF mode 1, so this realization was removed from the collection of sections and the EOF was recalculated.

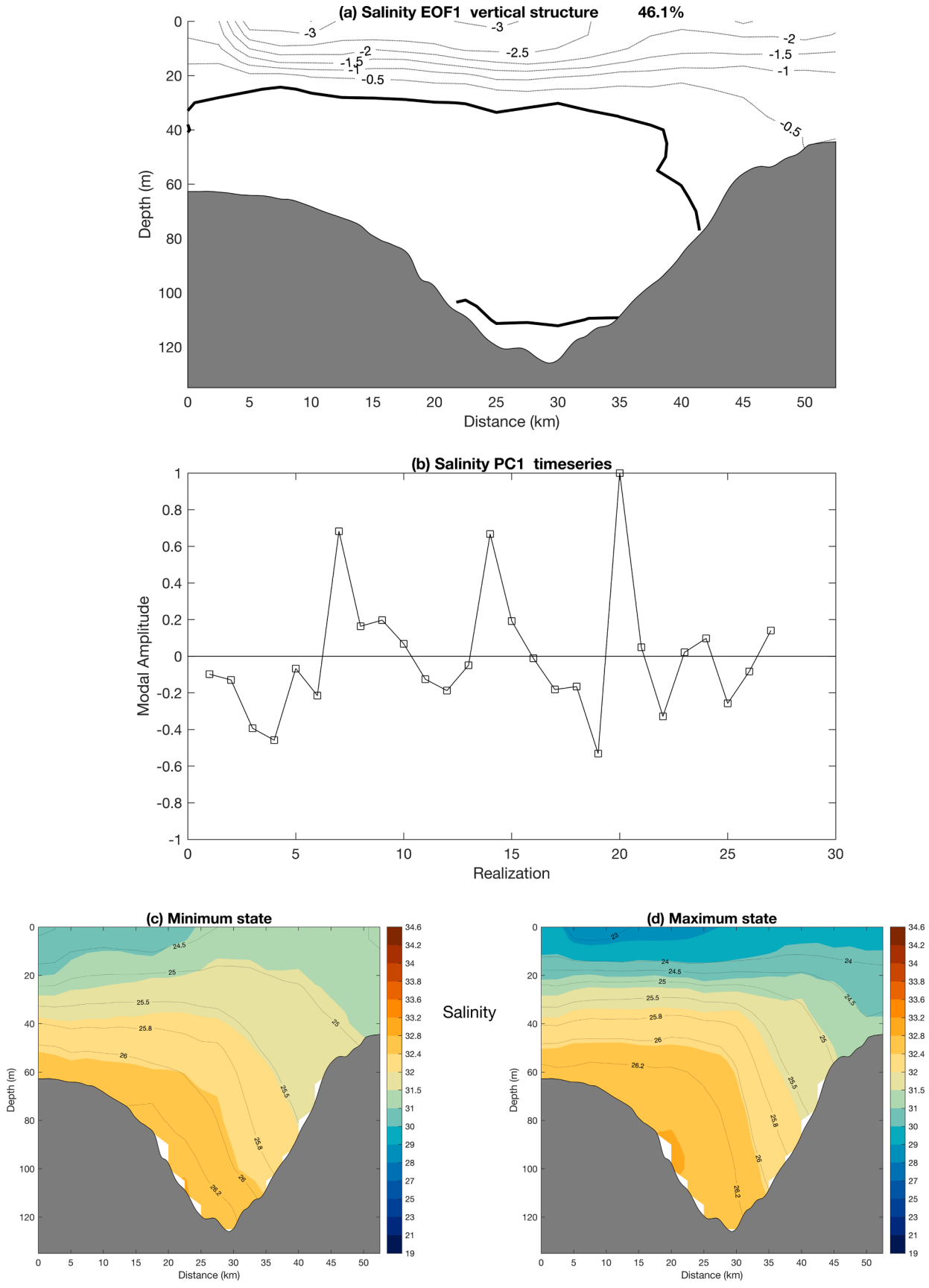

Fig. 10. Salinity EOF mode 1 for DBO5. (a) Vertical structure, where the contours represent the maximum dimensional amplitude of the mode. The percent variance explained by the mode is indicated. The bottom topography is from sound speed-corrected shipboard echosounder data. (b) Principal component timeseries plotted by section number (see text). (c) Minimum and maximum states of the EOF. The contours are density (kg m^{-3}).

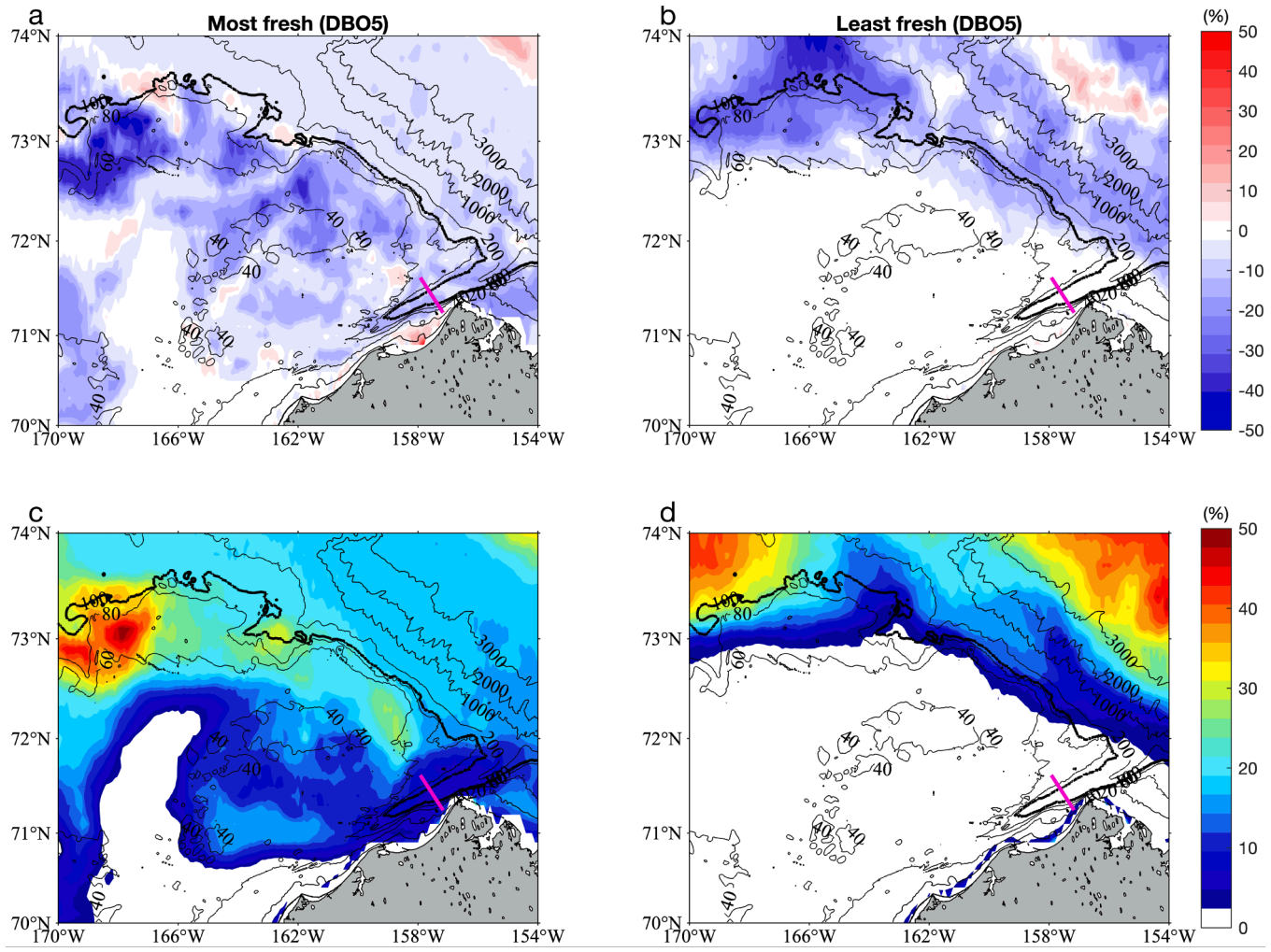

Fig. 11. Composite average ice maps corresponding to the two extremes of DBO5 EOF1 for salinity (see text for details). The top row is the net change in ice concentration over the 10-day period preceding the occupations of the sections, and the bottom row is the average ice concentration over that period. The left-hand column is for cases when the surface fresh layer is enhanced, and the right-hand column is for cases when the surface fresh layer is diminished. The bathymetry (in meters) is from IBCAOv3. The 100-m bathymetric contour is highlighted black. The magenta line is the DBO5 section.

point we are unable to ascribe a cause for this variation, although, based on the ERA5 data, we can say that it is not related to regional variations in the wind.

3.4. Mesoscale variability at DBO3 and Bering Strait

As documented earlier in Section 3.2, there is a seasonal signal in temperature and salinity at BS for both the ACC and CC Branch, captured by EOF1 (Fig. 8). Performing the same EOF calculation on the set of DBO3 sections[2], it is found that EOF1 for temperature also reflects the seasonal signal (as demonstrated above using the water mass approach in Fig. 9c,d). However, the dominant EOF for salinity (and density) does not reflect seasonality and is also not related to the ice melt signature present at DBO5. We now investigate the nature of the non-seasonal variation in salinity at DBO3 and BS, beginning with the former.

Fig 12 a-d shows the vertical structure and PC timeseries for first two EOF salinity modes at DBO3, which explain 27.5% and 23.5% of the variance, respectively. Mode 1 contains a broad region of negative amplitudes in the upper half of the water column with a small area of positive values near the coast (Fig. 12a), while mode 2 has a wedge of large negative values where the ACW is found on the inshore part of the section (Fig. 12c). In both cases the amplitudes are small on the western half of the line. Adding plus/minus one standard deviation back into the mean reveals how the two modes differ in their effect on the salinity field (Fig. 12e-h). Mode 1 corresponds to an offshore shift of lower salinity water resulting in a larger lateral salinity gradient in the central part of the section where the CC Branch resides (Fig. 12e,f). Note, however, that the minimum value of salinity near the eastern boundary remains approximately the same in the two states. By contrast, mode 2 is associated with strong freshening near the coast where the ACC is located (Fig. 12g,h). These results imply that mode 1 reflects changes in the CC Branch while mode 2 reflects changes in the ACC. Are there corresponding differences in the circulation? While we have no means to compute absolute geostrophic velocities associated with the different states, we can address the baroclinic flow.

To do this we computed the density EOF modes, which have nearly the same vertical structure and PC timeseries as the salinity modes. After adding plus/minus one standard deviation back into the mean for each mode, we computed the relative geostrophic velocity referenced to the bottom. The results are shown in Fig. 13. One sees that mode 1 corresponds to strengthening/weakening of the CC Branch, while the strength of the ACC remains approximately the same (it undergoes a small lateral shift, Fig. 13a,b). Conversely, in mode 2 the ACC strengthens/weakens

[2] The two realizations in September 2012 had anomalously fresh water present at the western end of the section that dominated the EOFs. As such, these realizations were removed and the EOF calculations re-done.

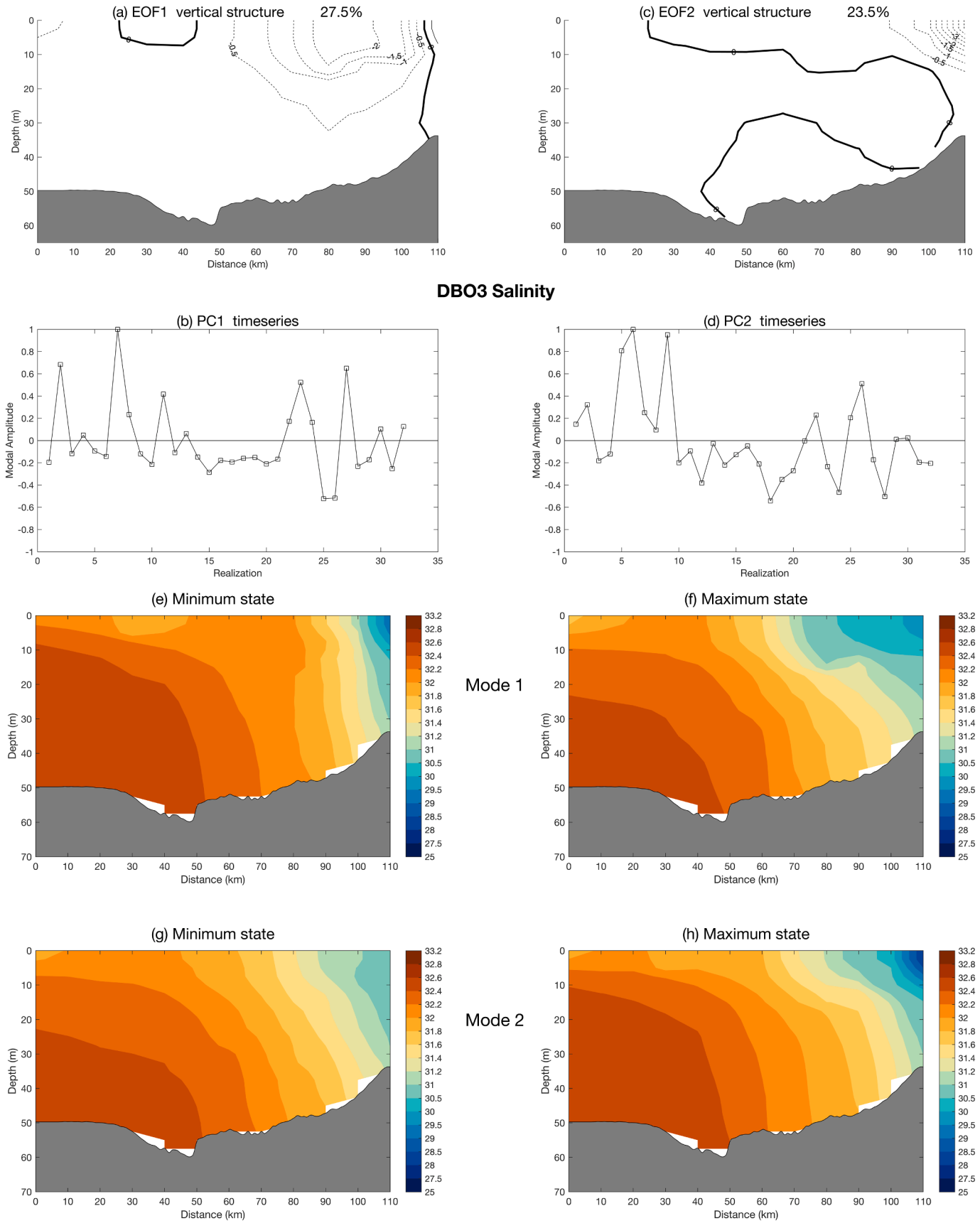

Fig. 12. Salinity EOF modes 1 and 2 for DBO3. (a,c) Vertical structure, where the contours represent the maximum dimensional amplitude of the mode. The percent variance explained by the mode is indicated. (b,d) Principal component timeseries. (e,f) Minimum and maximum states of mode 1. (g,h) Minimum and maximum states of mode 2. The bottom topography is from sound speed-corrected shipboard echosounder data.

significantly while the strength of the CC Branch changes by comparatively little (there is a lateral shift in the strongest flow, Fig. 13c,d). The corresponding volume transports bear this out. In mode 1 the CC Branch baroclinic transport approximately doubles while that of the ACC remains the same, and for mode 2 the ACC transport more than doubles while the CC Branch transport is nearly the same. We thus conclude that mode 1 reflects variability of the CC Branch, while mode 2 reflects variability in the ACC.

Regarding Bering Strait, recall that the dominant EOF for salinity is the seasonal signal. However, the next two modes (not shown) are analogous to the two EOF salinity modes for DBO3 described above: mode 2 is the ACC mode (23.4% variance explained) and mode 3 is the CC Branch mode (12.1% variance explained). Although only a relatively small amount variance is explained by the latter, this result implies that the same physical processes impacting the two flow branches are operating at both locations. The next question is, what are these processes?

As explained in Section 2.5, we removed the upwelling realizations from our set of sections at each site. However, the ACC mode identified here still appears to be wind-driven, albeit associated with weaker winds that are unable to initiate upwelling. We demonstrate this by constructing composite average maps of the 10-m wind field for the different extremes. At DBO3 we used the realizations whose PC values exceeded $\pm$ 0.5 times the standard deviation, and at BS we used the realizations exceeding $\pm$ 0.25 times the standard deviation (in order to increase the number of realizations there). Then, for each case, we computed the mean wind field over the two-day period preceding the occupation of the section (results are not sensitive to this exact choice). Finally, composite averages were made for the strong and weak ACC cases at each site.

This revealed an obvious connection between the wind field and the strength of the ACC (Fig. 14). At DBO3, the ACC is relatively strong when the winds are light, while the ACC is comparatively weak when the winds are out of the north and oppose the current (Fig. 14a,b). At BS, the ACC is relatively strong when the winds are out of the south, while the ACC is comparatively weak when the winds are light (Fig. 14c,d). We note that the specific wind conditions for the strong and weak ACC at the two sites are different because the times of the occupations at each location did not coincide. The salient point is that, outside of upwelling periods, the ACC varies as one would expect in response to moderately small variations in the wind. As such, the ACC mode identified here can be considered a mesoscale wind-driven mode. (We note that remote winds could also be playing a role via coastal shelf wave propagation; Danielson et al., 2014; 2020) At this point it remains unclear what the nature of the CC Branch mode is, as similarly constructed wind composites are inconclusive. This remains a topic of ongoing study.

3.5. *Northward evolution in the properties of the flow branches*

We now investigate how the water masses of the ACC and CC Branch change between Bering Strait and Barrow Canyon. First, at the three locations we computed the percentage of time that each water mass in Table 2 was present at every grid point across the section. We excluded the edges of the sections where there were fewer occupations because this skewed the percentages (whereas the mean quantities are not affected by a few missing occupations). The results are shown in Fig. 15. At BS the inshore part of the ACC is a mixture of MWM and ACW,

where the former is mostly confined to the upper 20 m. This makes

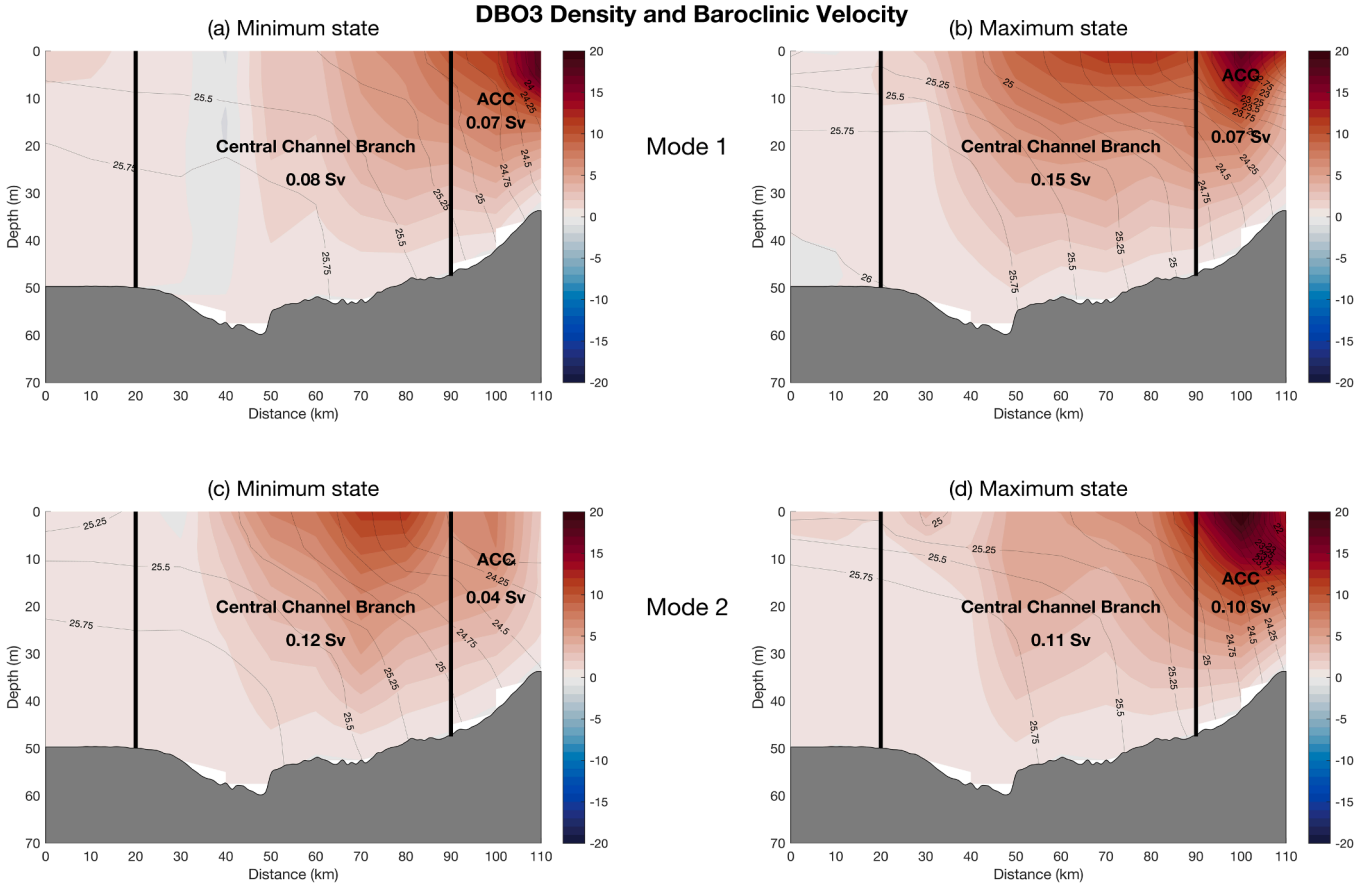

Fig. 13. Minimum and maximum states of the baroclinic velocity (color, cm s^{-1}) associated with density EOF modes 1 and 2 for DBO3 (contours, kg m^{-3}). The thick black lines delineate the Alaskan Coastal Current (ACC) and Central Channel Branch. The volume transports for each case are indicated. The bottom topography is from sound speed-corrected shipboard echosounder data.

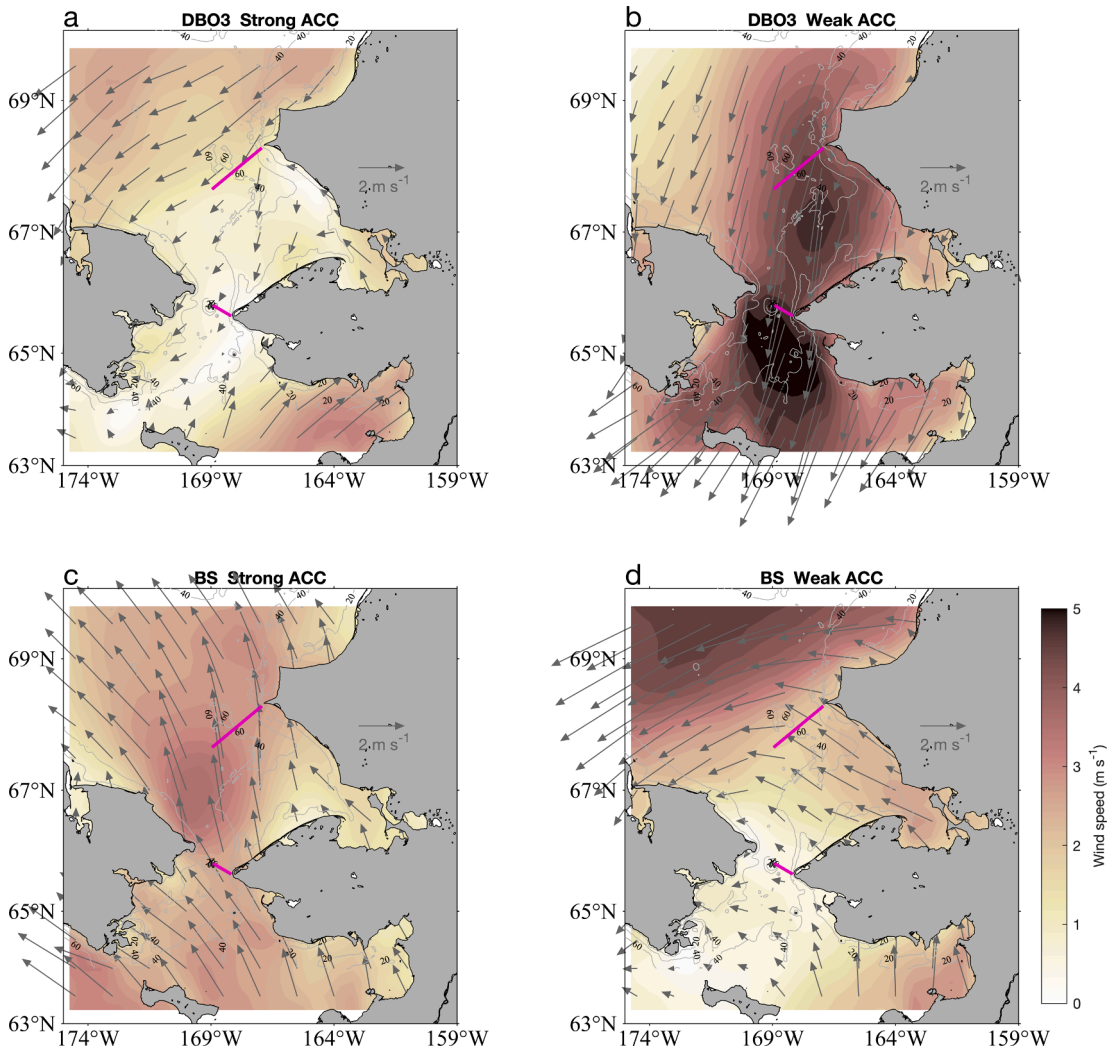

Fig. 14. Composite average maps of wind velocity (vectors) and speed (color) corresponding to the two extremes of the ACC mode for (a, b) DBO3 and (c, d) BS (see text for details). The magenta lines are the BS and DBO3 sections. The number of occupations that went into the composites are 8, 9, 7, 6 for panels a, b, c, d, respectively.

sense in that this is where the signature of continental runoff should be greatest. Seaward of the ACC there is a sharp transition to BSW which dominates the entire water column for the remainder of the section. By the location of DBO3, the MWM signature is all but gone and the ACC is now comprised mostly of ACW with a small amount of BSW. As was the case at BS, the CC Branch advects mostly BSW.

At the latitude of Barrow Canyon, the water mass situation has changed considerably. There is again a sizable presence of MWM in the upper layer, but now the percentage is greater seaward of the ACC. In line with the DBO5 salinity EOF results presented above, this is the signature of ice melt (i.e., cold MWM, see also Fig. 4b). A second big difference is that there is a sizable ACW presence across the upper part of the CC Branch. This is likely related to the fact that the isopycnals of the ACC no longer outcrop at this latitude, allowing for isopycnal spreading of this water mass. Finally, at DBO5 there is a significant presence of RWW and NVWW. This was shown in θ/S space in Fig. 4b; here we see that the deepest part of the CC Branch is dominated by these two cold water masses (Fig. 15, bottom row). The fact that they are concentrated on the western flank of Barrow Canyon is consistent with the notion, discussed earlier, that they have reached DBO5 via the long CC Branch pathway that flows around Hanna Shoal and drains into the west side of the canyon. Using a smaller collection of DBO5 sections, Pickart et al. (2019) found that most of the NVWW passed through Barrow Canyon during the month of August. Here we find that this coldest vintage of winter water is also sometimes present in July (only a single September occupation measured it).

3.5.1. *Alaskan Coastal current*

We now take a more detailed look at the northward evolution of the water advected by the ACC. As was done above in Section 3.2 to address the seasonality, we consider the average properties inshore of the ACC hydrographic front. Before doing this, however, we removed the extreme instances of mesoscale variability associated with ACC mode identified in the previous section – in particular, the realizations corresponding to the six most positive and six most negative PC values for the ACC mode at DBO3 and the five most positive and five most negative PC values for the ACC mode at BS (we removed fewer BS realizations because there were fewer BS sections overall). Supplementary Fig. 4 shows the effect that removing these extreme cases has on the ACW properties at DBO3 plotted in θ/S space[3]. The realizations in question include the freshest and coldest values, which, when excluded,

[3] The second realization in September 2012, which was not included in the DBO3 salinity/density EOF calculation due to the presence of anomalously fresh water at the western end of the section, also had anomalously fresh water in the ACC. Hence this realization was removed as well.

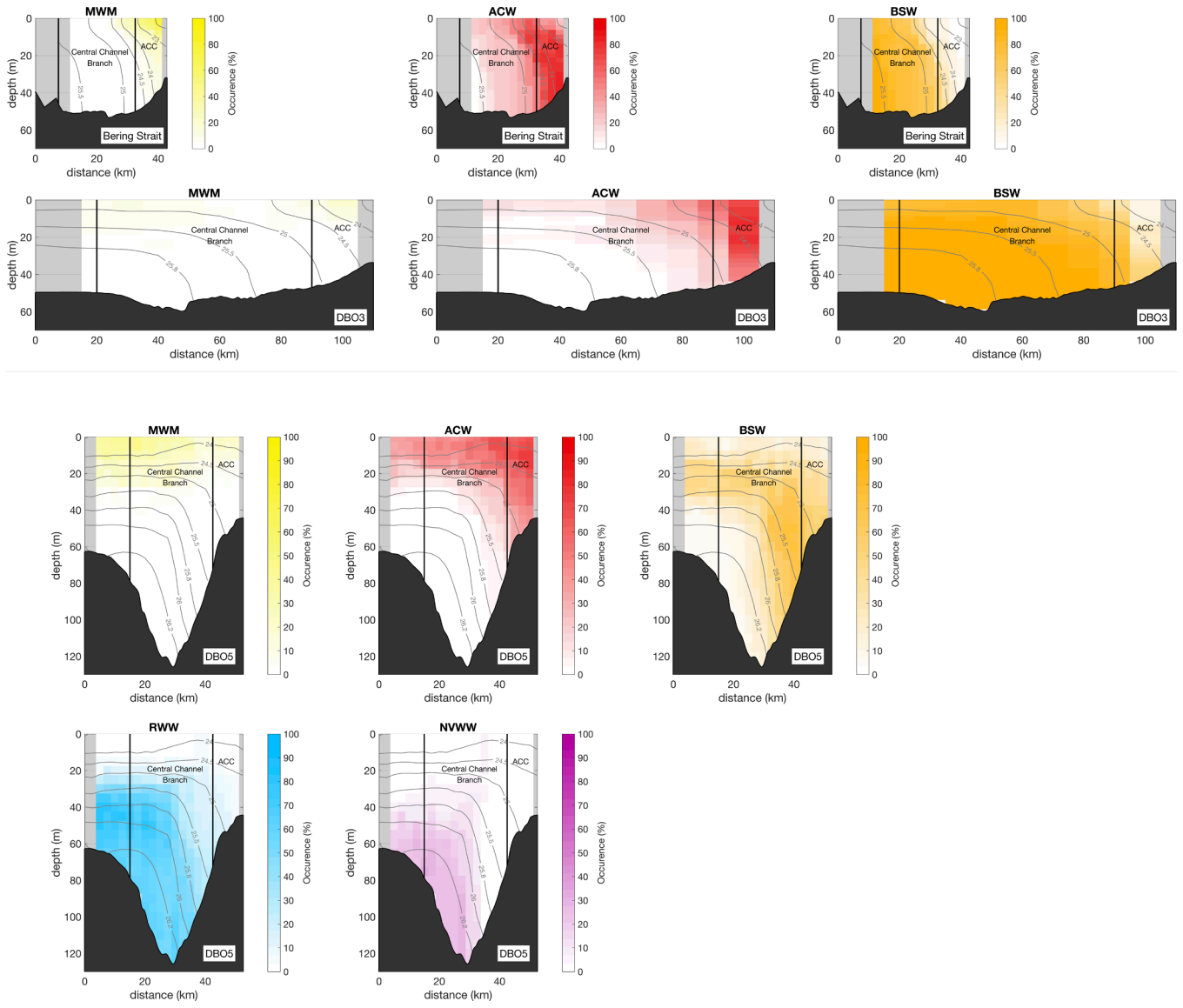

Fig. 15. Water mass percentage sections at (top row) Bering Strait, (second row) DBO3, (third and fourth row) DBO5. MWM = sea-ice melt water / meteoric water; ACW = Alaskan Coastal Water; BSW = Bering Summer Water; RWW = Remnant Winter Water; NVWW = Newly Ventilated Winter Water. Contours are the mean density (kg m^{-3}). The thick black lines delineate the Alaskan Coastal Current (ACC) and Central Channel Branch. The bottom topography is from sound speed-corrected shipboard echosounder data.

significantly reduce the scatter. For the ACC at DBO5 we removed the five most positive/negative PC values of the EOF mode associated with ice melt, which reduced the scatter at this location. We also excluded the October and November realizations at DBO5 due to strong air-sea forcing and ice formation at that time of year.

The resulting water mass properties of the ACC at the three different locations on the Chukchi shelf are documented in Fig. 16a. The small squares are the individual realizations, and the solid stars are the means of these values with the standard error indicated. These results suggest that, as the ACC progresses from BS to DBO3, it becomes saltier with little change in temperature. Then, from DBO3 to DBO5, the salinity increases further (although by a smaller amount) and the water becomes significantly colder. However, while the realizations at each line are

distributed fairly evenly over the summer months (supplementary Fig. 5), in order to track the water more accurately as it progresses northward, we need to account for the travel time of the ACC between the sites. To do this we estimated the path distances and used the mean northward velocity at the three sites from Fig. 5g-i. In particular, from BS to DBO3 we used a weighted average between the two sites with more weight given to the velocity at DBO3, since Bering Strait is a local constriction resulting in strong flow there. We used a similar weighed average for DBO3 and DBO5, with more weight given to DBO3 since Barrow Canyon is also a local constriction with strong flow. Supplementary Fig. 5 shows a Hovmöller plot of the data coverage (prior to early September) which includes the resulting path trajectory of the ACC starting in early July. On the plot we've marked three clusters of sections that were chosen in order to follow the current. The means of these three clusters are included in Fig. 16a as the open symbols. Qualitatively they tell the same story: from BS to DBO3 the biggest change is in salinity (the ACC gets saltier), and from DBO3 to DBO5 the biggest change is in temperature (the ACC gets colder). From hereon we use the values following the flow.

What dictates this evolution in properties? One obvious factor to consider is lateral mixing, which we assessed via the following simple calculation. Using the set of occupations at BS and DBO3, excluding the extreme ACC mode realizations, we constructed mean vertical sections of T, S, and density. Next, we defined a shoulder region immediately offshore of the ACC bounded by the ACC frontal isopycnal onshore and a

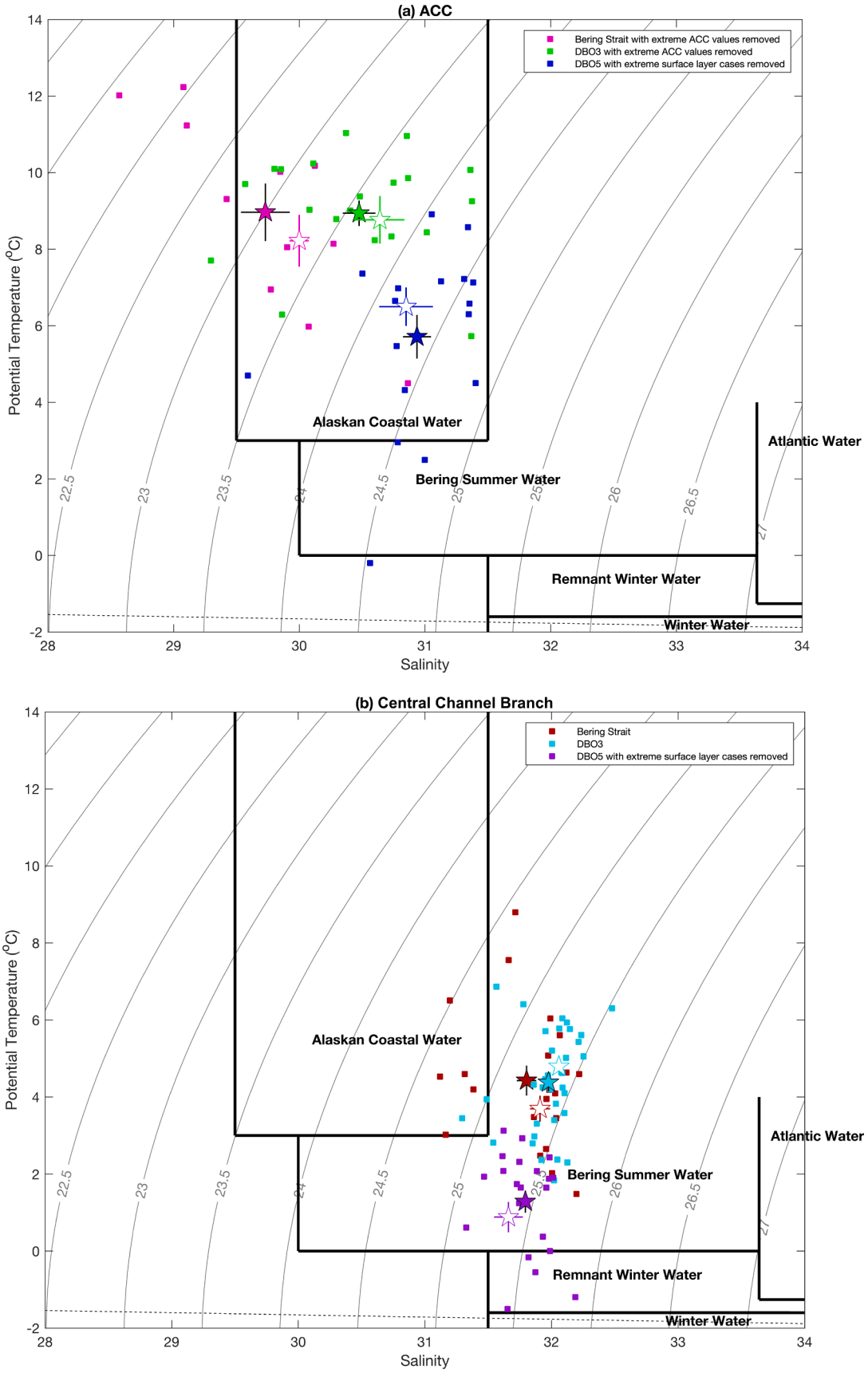

Fig. 16. Properties of the (a) ACC and (b) CC Branch as the currents progress northward across the Chukchi shelf. The different colors are associated with the three locations (see legend). The small solid squares are the values associated with the individual sections, and the large solid stars are the means for each location along with the standard errors. The open stars are the means accounting for the advective offsets between the locations (see text).

second isopycnal offshore such that the cross-stream width of the shoulder was approximately the same as the ACC (results are not sensitive to this exact choice). To estimate the effect of lateral mixing, we took the average between the mean ACC value and mean shoulder value at BS as the predicted ACC value at DBO3 (ignoring any effect from the inner part of Kotzebue Sound, which is taken to be negligible). This successfully explained the observed salinification from BS to DBO3 but predicted a drop in temperature of −0.9 °C versus the small observed increase of 0.5 °C (see Table 3). The analogous calculation from DBO3 to DBO5 again showed reasonably good agreement with respect to the salinification, but predicted a drop in temperature of only −0.9 °C versus the observed drop of −2.3 °C. This suggests that, to first order, lateral mixing can explain the evolution in salinity of the ACC but not the temperature.

For the period corresponding to most of our observations, 2010–2020, the path of the ACC was predominantly ice-free during the months of July and August. As such, summertime solar heating would be expected to warm the ACC as it progresses northward during these two months. We used the ERA5 reanalysis data to compute the climatological 2010–2020 mean daily open-water heat flux in the Chukchi Sea for the months of July-October. This consisted of the turbulent heat flux (sensible and latent) and the radiative heat flux (long wave and short wave). The bi-weekly means are shown in Fig. 17, which indicate that the ocean gains heat during July and most of August and loses heat in September and October. Acting alone, this would increase the temperature of the surface ACC water as it advects from BS to DBO5 (see the ACC trajectory in Fig. 17, where the water reaches DBO5 at the end of August). However, wind mixing will distribute this heat to depth.

To investigate this process and estimate the resulting change in ACC temperature, we used the 1-dimensional PWP mixing model described in Section 2.8. For the initial condition we used the mean hydrographic profile at the center of the ACC from the July cluster of sections at BS (see supplementary Fig. 5). We then subjected this profile to the local air-sea heat flux and wind stress as it progressed northward at the above-calculated ACC advective speed, leaving Bering Strait on 1 July (see Fig. 17). We used the 3-hourly ERA5 timeseries where the diurnal fluctuations in radiative forcing were smoothed out (which did not impact the results). We do not consider the surface freshwater fluxes since they are small and do not change the outcome (this was verified by including them in the initial set of calculations). The climatological mean daily heat flux and wind stress for 2010–2020 following the ACC northward are shown in Fig. 18a,c. The x-axis is time where the green dashed line indicates when the water passes the DBO3 line. For roughly two weeks after leaving Bering Strait the net air-sea heating is between −150 and −200 W m^{-2} (negative values correspond to ocean heating), decreasing steadily thereafter (Fig. 18a). Note that the turbulent heat loss has a larger impact as the summer progresses. The wind stress fluctuates around zero until early August, after which the winds are prevalently out of the northeast with larger values of (negative) wind stress (Fig. 18c).

Realizing that the surface forcing varies from year-to-year, we ran the PWP model for each year spanning 2010–2020 using the forcing for the corresponding year. We then considered the ensemble mean impact on the ACC temperature. For each run, the mixed layer is taken to be 5 m initially, and, as the water moves northward, the heating is confined to that depth until the first wind event mixes the signal deeper. Subsequent heating and vertical mixing can result in stacked mixed layers of different temperature. Recall that we have excluded the upwelling realizations from our study (it is during such wind events that the heat is mixed downwards). As such, our data reflect the re-stratified state of the ACC, i.e., the integrated impact of solar heating together with wind mixing. Therefore, in order to compare the PWP results to the data, we computed the vertically averaged temperature at each model time step from the surface to the depth of the deepest previous mixed layer (which on average was 16 ± 3 m by the end of the run). Since our observational averages often include water close to the bottom (depending on the penetration depth of the ACC frontal isopycnal), we also calculated the model average temperature over the full water column (40 m) at each time step.

The ensemble means of these two averages are shown in Fig. 18e, plotted as the change in temperature from the initial time. In the first case the net increase in temperature of the ACC from BS to DBO3 is 3.4 ± 0.3 °C, and in the second case it is 1.5 ± 0.1 °C (see also Table 4). The most reasonable comparison to the data is likely somewhere in between. As presented above, excluding the effect of lateral mixing (which the PWP model cannot address), our observations imply an increase in temperature of 1.4 ± 0.6 °C (i.e., 0.5 °C + 0.9 °C; Table 3). In light of the different factors involved in implementing the model and manipulating the data, as well as the observational uncertainty, this agreement is encouraging. It suggests that the observed evolution in ACC temperature from BS to DBO3 can be explained by a combination of lateral mixing together with solar heating and vertical wind mixing.

The same cannot be said for the evolution in ACC temperature from DBO3 to DBO5, as the temperature of the current dropped by −2.3 ± 0.6 °C according to the observations (open symbols in Fig. 18a; see also Table 3). The ensemble of PWP simulations imply that the temperature should increase by between 0.9 ± 0.1 °C and 1.9 ± 0.5 °C (Table 4), or, when taking lateral mixing into account, between 0.0 ± 0.1 °C and 1.0 ± 0.5 °C. We suspect that this discrepancy is due to the presence of the cold melt water in the northern Chukchi Sea. As noted above, the isopycnals in the ACC no longer outcrop at DBO5 (as they do at BS and DBO3). For instance, note the 24.5 kg m^{-3} isopycnal in Fig. 5. Using the historical hydrographic dataset (Section 2.9), we computed the climatological mean surface potential density for the period July-September. This revealed that, north of Cape Lisburne, the 24.5 kg m^{-3} isopycnal diverges from the coast, i.e., the isopycnal outcrops far seaward of the ACC. Hence, for most of its path from DBO3 to DBO5, the ACC can mix isopycnally with cold water. This is even more effective than the (diapycnal) lateral mixing to the south and would act to significantly cool the current. Note, however, that since the density is mostly dictated by salinity, such isopycnal mixing will have minimal impact on the salinity of the ACC.

Table 3
Observed change in properties of the ACC and CC Branch as the water flows northward across the Chukchi shelf. The predicted changes for the ACC due to lateral mixing are also shown (lateral mixing for the CC Branch is not considered, see text).

ACC Observations	Temperature change	Salinity change
Bering Strait to DBO3	0.5 ± 0.6 °C	0.64 ± 0.13
DBO3 to DBO5	−2.3 ± 0.6 °C	0.21 ± 0.20
CC Branch Observations	Temperature change	Salinity change
Bering Strait to DBO3	1.1±0.3 °C	0.15±0.05
DBO3 to DBO5	−3.9±0.3 °C	−0.40±0.07
ACC Lateral mixing	Predicted temperature change	Predicted salinity change
Bering Strait to DBO3	−0.90 °C	0.57
DBO3 to DBO5	−0.90 °C	0.34

3.5.2. Central Channel Branch

To address the northward evolution of the water advected by the CC Branch, we consider the average properties within the geographical limits of the current, as was done above in Section 3.2 for the seasonality. The results are shown in Fig. 16b, where the small squares are the individual realizations and solid stars are the means of these values with the standard error (we did not remove the extreme values of the CC Branch EOF modes at BS and DBO3, since this did not impact the scatter of values as it did for the ACC, and we kept the October and November realizations at DBO5 because of the longer travel time for the CC Branch

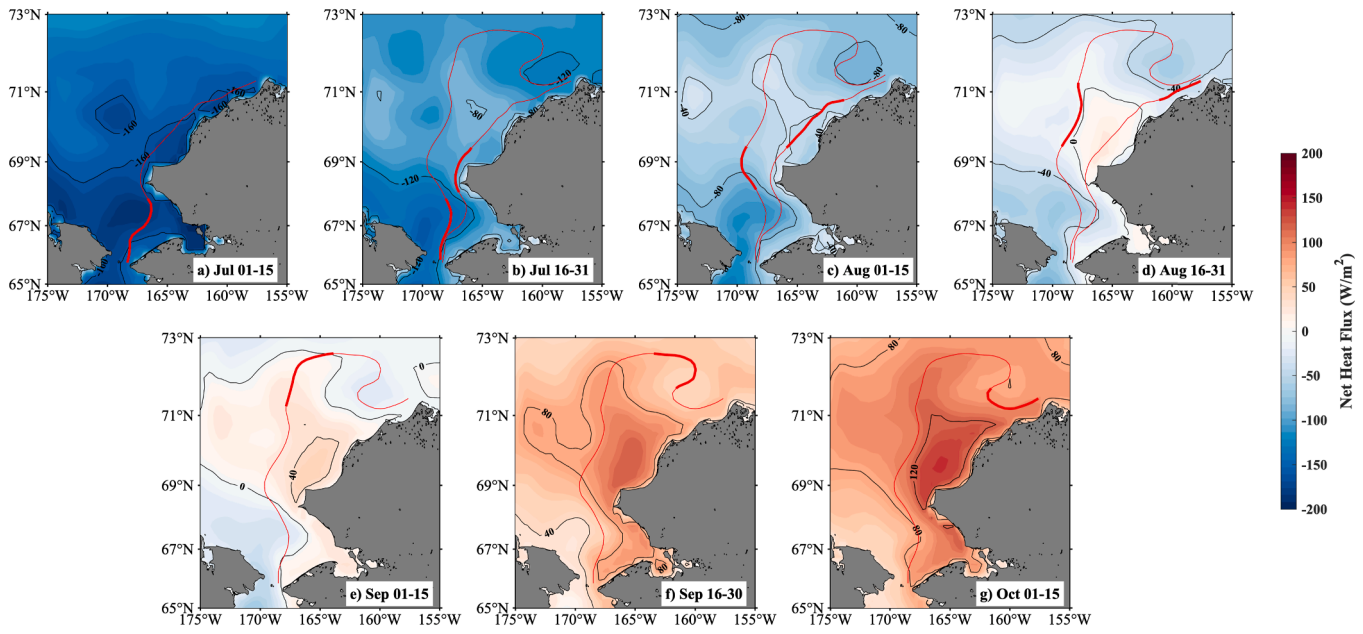

Fig. 17. 2010–2020 mean net heat flux (W/m$^{2)}$ from ERA5 for (a) July 1–15, (b) July 16–31, (c) August 1–15, (d) August 16–31, (e) September 1–15, (f) September 16–30, and (g) October 1–15. Negative flux means the ocean is gaining heat. The red curves mark the pathways of the ACC and CC Branch, with the thicker sections representing the location of the water leaving Bering Strait on 1 July for the ACC and 15 July for the CC Branch.

to reach Barrow Canyon). This suggests that there is little change in either temperature or salinity of the CC Branch between BS and DBO3. As with the ACC, we did another calculation accounting for the travel time of the CC Branch between the two sites. Again, we identified two clusters of sections (Supplementary Fig. 6) and computed the means (the open symbols in Fig. 16b). In this case, there is a still only a small change in salinity, but now the temperature increases between the two sites by 1.1 ± 0.3 °C (Table 3). From hereon we use the values following the flow. We note that lateral mixing would not be expected to change the properties of the CC Branch by much over this distance, since the current mixes with warmer/fresher water onshore and colder/saltier water offshore (whereas the ACC only mixes with colder/saltier water offshore).

The PWP calculation was done for the CC Branch trajectory in Fig. 17. This is the longest route that brings the water around the north side of Hanna Shoal before draining into Barrow Canyon (although the first part of the trajectory from BS to DBO3 is common to all of the CC Branch pathways). For the initial condition we computed an average BS section using the cluster of realizations from early July to early August (Supplementary Fig. 6), choosing a profile in the middle of the current. The calculation was initiated on July 15 (there were more realizations since the extreme EOF cases were not removed). The surface forcing following the water is shown in Fig. 18b,d. One sees that the net heat flux changed sign near the beginning of September, and there was sizable negative wind stress (northeasterly wind) north of DBO3. Accordingly, the two ensemble means of the PWP simulations (averaged to the deepest mixed layer depth (mean of 25 ± 4 m) and averaged to the bottom (55 m)), show that the temperature change of the CC Branch plateaus north of DBO3 and decreases thereafter (Fig. 18f). The predicted increase in temperature from BS to DBO3 is between 1.9 ± 0.2 °C and 0.9 ± 0.1 °C (Table 4), compared to the observed increase of 1.1 ± 0.3 °C (Table 3). Again, this agreement is encouraging.

From DBO3 to DBO5, the PWP model predicts that the temperature of the CC Branch should decrease between −1.1 ± 0.4 °C and −0.4 ± 0.2 °C. As seen in Supplementary Fig. 6, the appropriate cluster of sections to use at DBO5 is centered in mid-October, which gives an observed temperature decrease of −3.9 ± 0.3 °C (Table 3, although it should be kept in mind that there are only five DBO5 occupations during this time period). As was the case with the ACC, there is a large discrepancy between the observed decrease in temperature and that implied by air-sea heat flux plus wind mixing over this distance. It should be noted that all five of the October/November DBO5 sections contained some amount of RWW in the deep part of the CC Branch, which means that a portion of this water mass was still draining from the canyon via the long pathway around Hanna Shoal when the sections were occupied. This is at odds with the assumption of the advective calculation which follows the water (there was no RWW present at BS or DBO3). However, removing this deep RWW signal makes only a small difference. We surmise that the discrepancy is again due to presence of cold melt water on the northern part of the Chukchi shelf. This further highlights the importance of the seasonal ice melt on the properties of the two Pacific water flow branches as they progress towards the Arctic basin.

4. Summary

In this study we have used a unique set of shipboard hydrographic sections occupied by the scientific community as part of the Distributed Biological Observatory and Arctic Observing Network, together with a new climatology of shipboard ADCP data. The majority of the data were collected from 2010 to 2020 during the warm months of the year. Time periods of wind-driven upwelling were excluded from the study. This has allowed us, for the first time, to distinguish the two Pacific water flow branches in the eastern Chukchi Sea – the Alaskan Coastal Current (ACC) and Central Channel (CC) Branch. In the mean, mass was balanced for both currents at the three sampled locations: Bering Strait, seaward of Pt. Hope (DBO3), and in Barrow Canyon (DBO5). For the ACC, a seasonal signal was evident at Bering Strait where the current was warmest and freshest in September with a maximum in baroclinic transport, whereas the CC Branch displayed seasonality only in temperature. North of Bering Strait a seasonal signal was harder to discern, and in Barrow Canyon the dominant variability is consistent with yearly changes in sea ice melt in the northern Chukchi Sea shelf.

Mesoscale variability was evident at both Bering Strait and the DBO3 line. An EOF analysis revealed an ACC mode and a CC Branch mode. In the former, which is associated with moderate changes in the wind, the ACC varies between a colder, fresher state with enhanced baroclinic transport, and a relatively warmer, saltier state with diminished

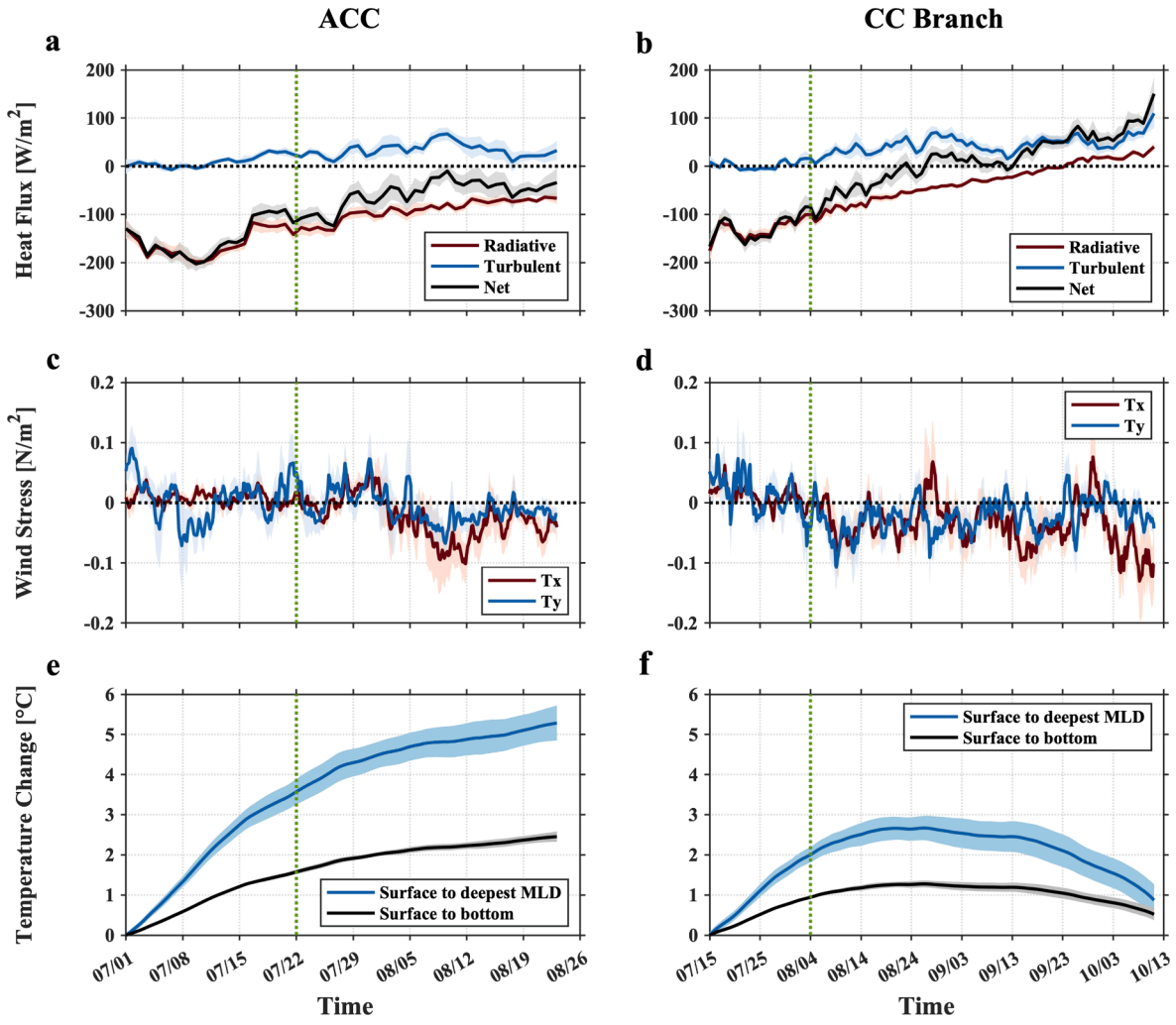

Fig. 18. (a, b) Timeseries of air-sea heat flux; (c, d) wind stress; and (e, f) PWP simulated temperature change along the pathway of the ACC (left panels) and CC Branch (right panels). The temperature change is relative to the initial temperature at Bering Strait. The solid line and shading represent mean and standard error, respectively. The green dashed line indicates the time when the water arrives at the DBO3 line, and the plots end at the DBO5 line.

Table 4
Results from the PWP simulations.

ACC PWP	Temperature change averaged from the surface to deepest MLD	Temperature change averaged from the surface to Bottom
Bering Strait to DBO3	3.4 ± 0.3 °C	1.5 ± 0.1 °C
DBO3 to DBO5	1.9 ± 0.5 °C	0.9 ± 0.1 °C
CC PWP	Temperature change averaged from the surface to deepest MLD	Temperature change averaged from the surface to Bottom
Bering Strait to DBO3	1.9 ±0.2 °C	0.9±0.1 °C
DBO3 to DBO5	−1.1±0.4 °C	−0.4±0.2 °C

baroclinic transport. The CC Branch mode is associated with increased/decreased baroclinic transport, with the core of the current located farther offshore in the former state. We were unable to identify an underlying cause of this mode, although it does not appear to be wind-driven. The change in hydrographic properties of both currents were investigated in an advective framework following the flow. The northward increase in salinity of the ACC can be explained by lateral mixing alone, but solar heating together with wind mixing play a large role in the temperature evolution. This same atmospheric forcing also impacts the CC Branch. However, the large observed decrease in temperature of both currents between Pt. Hope and Barrow Canyon appears to be due to the influence of sea-ice melt water on the northern Chukchi shelf. This notion warrants further investigation, especially in light of the ongoing changes in seasonal ice cover due to the warming climate.

Declaration of Competing Interest

The authors declare that they have no known competing financial interests or personal relationships that could have appeared to influence the work reported in this paper.

Data availability

There is a data availability section with links.

Acknowledgements

The authors are indebted to the many research vessels and their crews, along with the large number of technicians, who collected and processed the data that formed the foundation of this study. We acknowledge R. Woodgate, C. Peralta-Ferriz, and the Bering Strait Mooring Program (currently funded by the National Science Foundation Arctic Observing Network) for use of the Bering Strait mooring and shipboard hydrographic data.

Funding for the shipboard measurements came from many sources, including: the US National Science Foundation; the US National Oceanic and Atmospheric Administration; the US Office of Naval Research; the US National Aeronautics and Space Administration Biology Program; the US Bureau of Ocean Energy Management; the US Alaska Ocean Observing System; the Shanghai Pujiang Program (22PJ1406400), Shanghai Frontiers Science Center of Polar Science (SCOPS); the Korea Institute of Marine Science & Technology Promotion (KIMST) funded by the Ministry of Oceans and Fisheries (20210605, KOPRI); Ministry of Education, Culture, Sports, Science and Technology Japan (JPMXD1420318865); the Natural Sciences and Engineering Research Council of Canada; Fisheries and Oceans, Canada.

Data Availability

The links to the CTD data used in the study are listed in Supplementary Table 1.

The ERA5 air–sea heat flux and wind stress data are available at https://www.ecmwf.int/en/forecasts/datasets/reanalysis- datasets/era5.

The University of Bremen sea ice concentration data are available at https://seaice.uni-bremen.de/.

The Bering Strait mooring data are available at http://psc.apl.washington.edu/HLD/Bstrait/Data/BeringStraitMooringDataArchive.html.

The data for mooring BC2 are available at https://data.eol.ucar.edu/dataset/62.316.

The data for mooring MC6 are available at http://psc.apl.washington.edu/HLD/Chukchi/Chukchi.html.

The historical hydrographic data are available from the following sources: (1) Unified Database for Arctic and Subarctic Hydrography (https://doi.pangaea.de/10.1594/PANGAEA.872931); (2) World Ocean Database 2018 (https://www.ncei.noaa.gov/products/ world-ocean-database); (3) Arctic Data Center (https://arcticdata.io/ catalog/data); (4) Beaufort Gyre Exploration Project (https://www2. whoi.edu/site/beaufortgyre/data/data-overview/); (5) Pacific Marine Environmental Laboratory (https://www.pmel.noaa.gov/data-links); (6) NOAA Alaska Fisheries Science Center (https://data.eol.ucar.edu/ dataset/); (7) University of Alaska Fairbanks Institute of Marine Science (available at the Arctic Ocean Observing System, http://www.aoos.org); (8) Fisheries and Oceans Canada's Institute of Ocean Sciences (https://www.dfo-mpo.gc.ca/science/publications/index-eng.htm); (9) JAMSTEC (http://www.godac.jamstec.go.jp/darwin/e/); and (10) Korea Polar Data Center (https://kpdcopen.kopri.re.kr).

The ChukSA climatology of shipboard ADCP are available from the NCEI repository: https://www.ncei.noaa.gov/access/metadata/landing-page/bin/iso?id = gov.noaa.nodc:0283043.

Appendix A. Supplementary data

Supplementary data to this article can be found online at https://doi.org/10.1016/j.pocean.2023.103169.

References

Aagaard, K., Coachman, L. K., and Carmack, E. (1981). On the halocline of the Arctic Ocean. Deep-Sea Research, Part A. Oceanographic Research Papers 28 (6),529–545. https://doi.org/10.1016/0198-0149(81)90115-1.

Aagaard, K., Roach, A.T., Schumacher, J.D., 1985. On the wind-driven variability of the flow through Bering Strait. J. Geophys. Res. Oceans 90 (C4), 7213–7221. https://doi.org/10.1029/JC090iC04p07213.

Anderson, D. M., Fachon, E., Pickart, R. S., Lin, P., Fischer, A. D., Richlen, M. L., Uva, V., Brosnahan, M. L., McRaven, L., Bahr, F., Lefebvre, K., Grebmeier, J. M., Danielson, S. L., Lyu, Y., and Fukai, Y. (2021). Evidence for massive and recurrent toxic blooms of *Alexandrium catenella* in the Alaskan Arctic. Proceedings of the National Academy of Sciences, 118 (41), e2107387118. ttps://doi.org/10.1073/pnas.2107387118.

Bahr, F., McRaven, L.T., Pickart, R.S. (2023). ChukSA Climatology, Version 1.0: Ocean velocity profiles collected by ADCP in the Chukchi Sea, Bering Strait, and Bering Sea in 2002-2022 (NCEI Accession 0283043). NOAA National Centers for Environmental Information. Dataset. DOI: https://doi.org/10.25921/q8rx-9r22. Accessed 09/27/2023.

Behrendt, A., Sumata, H., Rabe, B., and Schauer, U. (2018). UDASH - Unified database for Arctic and subarctic hydrography. Earth System Science Data, 10:1119–1138. ttps://doi.org/10.5194/essd-10-1119-2018.

Coachman, L.K., Aagaard, K., Tripp, R., 1975. Bering Strait: The regional physical oceanography. University of Washington Press 29 (3), 129–180. https://doi.org/10.14430/arctic3020.

Cooper, L.W., Whitledge, T.E., Grebmeier, J.M., Weingartner, T.J., 1997. The nutrient, salinity, and stable oxygen isotope composition of Bering and Chukchi Seas waters in and near the Bering Strait. J. Geophys. Res. 102 (C6), 12563–12573. https://doi.org/10.1029/97JC00015.

Corlett, W.B., Pickart, R.S., 2017. The Chukchi Slope Current. Prog. Oceanogr. 153, 50–65. https://doi.org/10.1016/j.pocean.2017.04.005.

Danielson, S.L., Weingartner, T.J., Hedstrom, K.S., Aagaard, K., Woodgate, R.A., Curchitser, E., Stabeno, P.J., 2014. Coupled wind-forced controls of the Bering-Chukchi shelf circulation and the Bering Strait throughflow: Ekman transport, continental shelf waves, and variations of the Pacific-Arctic sea surface height gradient. Prog. Oceanogr. 125, 40–61. https://doi.org/10.1016/j.pocean.2014.04.006.

Danielson, S.L., Eisner, L., Ladd, C., Mordy, C., Sousa, L., Weingartner, T.J., 2017. A comparison between late summer 2012 and 2013 water masses, macronutrients, and phytoplankton standing crops in the northern Bering and Chukchi Seas. Deep Sea Res. Part II 135, 7–26.

Danielson, S.L., Ahkinga, O., Ashjian, C., Basyuk, E., Cooper, L.W., Eisner, L., Farley, E., Iken, K.B., Grebmeier, J.M., Juranek, L., Khen, G., Jayne, S.R., Kikuchi, T., Ladd, C., Lu, K., Mccabe, R.M., Moore, G.W.K., Nishino, S., Ozenna, F., Pickart, R.S., Polyakov, I., Stabeno, P.J., Thoman, R., Williams, W.J., Wood, K., Weingartner, T.J., 2020. Manifestation and consequences of warming and altered heat fluxes over the Bering and Chukchi Sea continental shelves. Deep Sea Res. Part II 104781. https://doi.org/10.1016/j.dsr2.2020.104781.

Y.C. Fang T.J. Weingartner E.L. Dobbins P. Winsor H. Statscewich R.A. Potter T.D. Mudge C.A. Stoudt K. Borg Circulation and thermohaline variability of the Hanna shoal region on the northeastern Chukchi Sea shelf Journal of Geophysical Research: Oceans 125 2020 e2019JC015639 10.1029/2019JC015639.

Gong, D. and Pickart, R. S. (2016). Early summer water mass transformation in the eastern Chukchi sea. Deep-Sea Research Part II: Topical Studies in Oceanography, 130:43–55. .

Grebmeier, J. M., Bluhm, B. A., Cooper, L. W., Danielson, S. L., Arrigo, K. R., Blanchard, A. L., Clarke, J. T., Day, R. H., Frey, K. E., and Gradinger, R. R. (2015). Ecosystem characteristics and processes facilitating persistent macrobenthic biomass hotspots and associated benthivory in the Pacific Arctic, Progress in Oceanography, 136, 92-114.

Grebmeier, J.M., Frey, K.E., Cooper, L.W., Kędra, M., 2018. Trends in benthic macrofaunal populations, seasonal sea ice persistence, and bottom water temperatures in the Bering Strait region. Oceanography 31 (2). https://doi.org/10.5670/oceanog.2018.224.

Hersbach, H., Bell, B., Berrisford, P., Biavati, G., Horányi, A., Muñoz Sabater, J. Nicolas, J., Peubey, C., Radu, R., Rozum, I., and Schepers, D. (2018). ERA5 hourly data on single levels from 1959 to present . Copernicus Climate Change Service (C3S) Climate Data Store (CDS), 10(10.24381).

Hirano, D., Fukamachi, Y., Watanabe, E., Ohshima, K.I., Iwamoto, K., Mahoney, A.R., Eicken, H., Simizu, D., Tamura, T., 2016. A wind-driven, hybrid latent and sensible heat coastal polynya off Barrow, Alaska. J. Geophys. Res.: Oceans 121 (1), 980–997. https://doi.org/10.1002/2015JC011318.

Huang, J., Pickart, R.S., Chen, Z., Huang, R.X., 2023. Role of air-sea heat flux on the transformation of Atlantic water encircling the Nordic Seas. Nat. Commun. 14, 141. https://doi.org/10.1038/s41467-023-35889-3.

Itoh, M., Nishino, S., Kawaguchi, Y., Kikuchi, T., 2013. Barrow Canyon volume, heat, and freshwater fluxes revealed by long-term mooring observations between 2000 and 2008. J. Geophys. Res. Oceans 118, 4363–4379. https://doi.org/10.1002/jgrc.20290.

Ladd, C., Mordy, C., Salo, S., Stabeno, P., 2016. Winter water properties and the Chukchi Polynya. J. Geophys. Res. Oceans 121 (8), 5516–5534. https://doi.org/10.1002/2016JC011918.

Li, S., Lin, P., Dou, T., Xiao, C., Itoh, M., Kikuchi, T., & Qin, D. (2022). Upwelling of Atlantic water in Barrow Canyon, Chukchi Sea. Journal of Geophysical Research: Oceans, 127(3), e2021JC017839. https://doi.org/10.1029/2021JC017839.

Li, J., Lin, P., Pickart, R.S., Yang, X.Y., 2021. Time dependent flow of Atlantic water on the continental slope of the Beaufort Sea based on moorings. J. Geophys. Res. Oceans 126. https://doi.org/10.1029/2020JC016996.

Li, M., Pickart, R.S., Spall, M.A., Weingartner, T.J., Lin, P., Moore, G.W., Qi, Y., 2019. Circulation of the Chukchi Sea shelfbreak and slope from moored timeseries. Prog. Oceanogr. 172 (3), 14–33. https://doi.org/10.1016/j.pocean.2019.01.002.

Lin, P., Pickart, R. S., Våge, K., and Li, J. (2021). Fate of warm Pacific water in the Arctic basin, Geophysical Research Letters, 48(20), e2021GL094693. https://doi.org/10.1029/2021GL094693.

Lin, P., Pickart, R.S., McRaven, L.T., Arrigo, K.R., Bahr, F., Lowry, K.E., Stockwell, D.A., Mordy, C.W., 2019. Water mass evolution and circulation of the northeastern Chukchi Sea in summer: Implications for nutrient distributions. J. Geophys. Res. Oceans 124, 4416–4432. https://doi.org/10.1029/2019JC015185.

Lowry, K.E., Pickart, R.S., Mills, M.M., Brown, Z.W., van Dijken, G.L., Bates, N.R., Arrigo, K.R., 2015. The influence of winter water on phytoplankton blooms in the Chukchi Sea. Deep-Sea Research Part II: Topical Studies in Oceanography 118 (A), 53–72. https://doi.org/10.1016/j.dsr2.2015.06.006.

Lowry, K.E., Pickart, R.S., Selz, V., Mills, M.M., Pacini, A., Lewis, K.M., Joy-Warren, H.L., Nobre, C., van Dijken, G.L., Grondin, P.L., Ferland, J., Arrigo, K.R., 2018. Under-ice phytoplankton blooms inhibited by spring convective mixing in refreezing leads. J. Geophys. Res. Oceans 123 (1), 90–109. https://doi.org/10.1002/2016JC012575.

Lu, K., Danielson, S., Hedstrom, K., Weingartner, T., 2020. Assessing the role of oceanic heat fluxes on ice ablation of the central Chukchi Sea Shelf. Prog. Oceanogr. 184, 102313 https://doi.org/10.1016/j.pocean.2020.102313.

Moore, S.E., Grebmeier, J.M., 2018. The Distributed Biological Observatory: Linking Physics to Biology in the Pacific Arctic Region. Arctic, 71. SUPPL 1, 1–7. https://doi.org/10.14430/arctic4606.

Mountain, D.G., Coachman, L.K., Aagaard, K., 1976. On the flow through Barrow Canyon. J. Phys. Oceanogr. 6 (4), 461–470. https://doi.org/10.1175/1520-0485(1976)006<0461:OTFTBC>2.0.CO;2.

Pacini, A., Moore, G.W., Pickart, R.S., Nobre, C., Bahr, F., Våge, K., Arrigo, K.R., 2019. Characteristics and transformation of pacific winter water on the Chukchi Sea shelf in late spring. J. Geophys. Res. Oceans 124, 7153–7177. https://doi.org/10.1029/2019JC015261.

Padman, L., Erofeeva, S., 2004. A barotropic inverse tidal model for the Arctic Ocean. Geophys. Res. Lett. 31 (2) https://doi.org/10.1029/2003GL019003.

Paquette, R.G., Bourke, R.H., 1974. Observations on the coastal current of Arctic Alaska. J. Mar. Res. 32 (2), 195–207. https://elischolar.library.yale.edu/journal_of_marine_research/1286.

Pickart, R.S., Pratt, L.J., Torres, D.J., Whitledge, T.E., Proshutinsky, A.Y., Aagaard, K., Agnew, T.A., Moore, G.W.K., Dail, H.J., 2010. Evolution and dynamics of the flow through Herald Canyon in the western Chukchi Sea. Deep-Sea Research Part II: Topical Studies in Oceanography 57, 5–26. https://doi.org/10.1016/j.dsr2.2009.08.002.

Pickart, R.S., Moore, G.W., Mao, C., Bahr, F., Nobre, C., Weingartner, T.J., 2016. Circulation of winter water on the Chukchi shelf in early summer. Deep-Sea Research Part II: Topical Studies in Oceanography 130, 56–75. https://doi.org/10.1016/j.dsr2.2016.05.001.

Pickart, R.S., Nobre, C., Lin, P., Arrigo, K.R., Ashjian, C.J., Berchok, C., Cooper, L.W., Grebmeier, J.M., Hartwell, I., He, J., Itoh, M., Kikuchi, T., Nishino, S., Vagle, S., 2019. Seasonal to mesoscale variability of water masses and atmospheric conditions in Barrow Canyon, Chukchi Sea. Deep-Sea Research Part II: Topical Studies in Oceanography 162, 32–49. https://doi.org/10.1016/j.dsr2.2019.02.003.

Pisareva, M. N., Pickart, R. S., Spall, M. A., Nobre, C., Torres, D. J., Moore, G. W. K., & Whitledge, T. E. (2015). Flow of Pacific water in the western Chukchi Sea: Results from the 2009 RUSALCA expedition. Deep Sea Research Part I: Oceanographic Research Papers, 105, 53-73. https://doi.org/10.1016/j.dsr.2015.08.011Get rights and content.

Pisareva, M.N., Pickart, R.S., Lin, P., Fratantoni, P.S., Weingartner, T.J., 2019. On the nature of wind-forced upwelling in Barrow Canyon. Deep-Sea Research Part II: Topical Studies in Oceanography 162, 63–78. https://doi.org/10.1016/j.dsr2.2019.02.002.

Price, J.F., Weller, R.A., Pinkel, R., 1986. Diurnal cycling: Observations and models of the upper ocean response to diurnal heating, cooling, and wind mixing. J. Geophys. Res. 91, 8411–8427. https://doi.org/10.1029/JC091iC07p08411.

Proshutinsky, A., Krishfield, R., Toole, J. M., Timmermans, M.-L., Williams, W., Zimmermann, S., Yamamoto-Kawai, M., Armitage, T. W., Dukhovskoy, D., Golubeva, E., Manucharyan, G. E., Platov, G., Watanabe, E., Kikuchi, T., Nishino, S., Itoh, M., Kang, S. H., Cho, K. H., Tateyama, K., and Zhao, J. (2019). Analysis of the Beaufort gyre freshwater content in 2003–2018. J. Geophys. Res.: Oceans, 124:9658–9689. https://doi.org/10.1029/2019JC015281.

Shroyer, E.L., Pickart, R.S., 2019. Pathways, timing, and evolution of Pacific winter water through Barrow Canyon. Deep-Sea Research Part II: Topical Studies in Oceanography 162, 50–62. https://doi.org/10.1016/j.dsr2.2018.05.004.

Spall, M.A., Pickart, R.S., Li, M., Itoh, M., Lin, P., Kikuchi, T., Qi, Y., 2018. Transport of Pacific water into the Canada Basin and formation of the Chukchi Slope Current. J. Geophys. Res. 123, 7453–7471. https://doi.org/10.1029/2018JC013825.

Stabeno, P.J., McCabe, R.M., 2023. Re-examining flow pathways over the Chukchi Sea continental shelf. Deep-Sea Research Part II: Topical Studies in Oceanography 207, 105243. https://doi.org/10.1016/j.dsr2.2022.105243.

Tian, F., Pickart, R. S., Lin, P., Pacini, A., Moore, G. W., Stabeno, P., Weingartner, T., Itoh, M., Kikuchi, T., Dobbins, E., Bell, S., Woodgate, R. A., Danielson, S. L., and Wang, Z. (2021). Mean and seasonal circulation of the eastern Chukchi Sea from moored timeseries in 2013–2014. J. Geophys. Res.: Oceans, 126, e2020JC016863. .

Weingartner, T., Aagaard, K., Woodgate, R., Danielson, S., Sasaki, Y., Cavalieri, D., 2005. Circulation on the north central Chukchi Sea shelf. Deep-Sea Research Part II: Topical Studies in Oceanography 52 (24–26), 3150–3174. https://doi.org/10.1016/j.dsr2.2005.10.015.

Weingartner, T.J., Danielson, S., Sasaki, Y., Pavlov, V., Kulakov, M., 1999. The Siberian Coastal Current: A wind- and buoyancy-forced arctic coastal current. J. Geophys. Res. Oceans 104, 29697–29713. https://doi.org/10.1029/1999JC900161.

Weingartner, T., Fang, Y.C., Winsor, P., Dobbins, E., Potter, R., Statscewich, H., Mudge, T., Irving, B., Sousa, L., Borg, K., 2017. The summer hydrographic structure of the Hanna Shoal region on the northeastern Chukchi Sea shelf: 2011–2013. Deep-Sea Research Part II: Topical Studies in Oceanography 144, 6–20. https://doi.org/10.1016/j.dsr2.2017.08.006.

Woodgate, R.A., 2018. Increases in the Pacific inflow to the Arctic from 1990 to 2015, and insights into seasonal trends and driving mechanisms from year-round Bering Strait mooring data. Prog. Oceanogr. 160, 124–154. https://doi.org/10.1016/j.pocean.2017.12.007.

Woodgate, R.A., Aagaard, K., Weingartner, T.J., 2005. A year in the physical oceanography of the Chukchi Sea: Moored measurements from autumn 1990–1991. Deep Sea Res. Part II 52 (24–26), 3116–3149. https://doi.org/10.1016/j.dsr2.2005.10.016.

R.A. Woodgate C. Peralta-Ferriz Warming and Freshening of the Pacific Inflow to the Arctic from 1990–2019 implying dramatic shoaling in Pacific Winter Water ventilation of the Arctic water column Geophysical Research Letters 48 9 2021 e2021GL092528 10.1029/2021GL092528.

Woodgate, R.A., Stafford, K.M., Prahl, F.G., 2015. A synthesis of year-round interdisciplinary mooring measurements in the Bering Strait (1990–2014) and the RUSALCA years (2004–2011). Oceanography 28 (3), 46–67. https://doi.org/10.5670/oceanog.2015.57.